Cell Reports

Article

Intrauterine Pressures Adjusted by Reichert's Membrane Are Crucial for Early Mouse Morphogenesis

Graphical Abstract

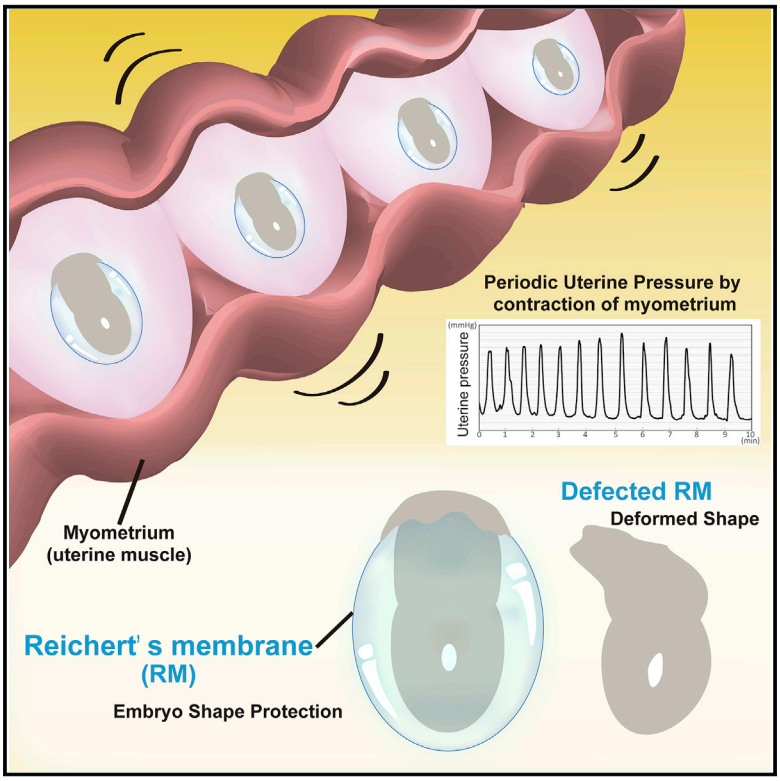

Authors

Yoko Ueda, Chiharu Kimura-Yoshida, Kyoko Mochida, ..., Olivier Lefebvre, Ryuji Hiramatsu, Isao Matsuo

Correspondence

imatsuo@wch.opho.jp

In Brief

Ueda et al. reveal that intrauterine pressures produced by uterine smooth muscle contractions show the highest and most frequent periodic peaks just after mouse embryo implantation. Reichert's membrane, a specialized basement membrane that wraps around the implanted embryo, plays a crucial role as a shock absorber of intrauterine pressures.

Highlights

- Smooth muscle contractions exert high and periodic intrauterine pressures on embryos
- Buffer space made by Reichert's membrane protects embryos from intrauterine pressures
- Intrauterine pressures are necessary to specify distal visceral endoderm correctly
- Reduced pressures restore the deformed shape of Reichert's-membrane-deficient embryos

Ueda et al., 2020, Cell Reports *31*, 107637
May 19, 2020
https://doi.org/10.1016/j.celrep.2020.107637

CellPress

Cell Reports

CellPress
OPEN ACCESS

Article

Intrauterine Pressures Adjusted by Reichert's Membrane Are Crucial for Early Mouse Morphogenesis

Yoko Ueda,[1] Chiharu Kimura-Yoshida,[1] Kyoko Mochida,[1] Mami Tsume,[1] Yoshitaka Kameo,[2] Taiji Adachi,[2] Olivier Lefebvre,[3] Ryuji Hiramatsu,[1,4] and Isao Matsuo[1,5,*]

[1]Department of Molecular Embryology, Research Institute, Osaka Women's and Children's Hospital, Osaka Prefectural Hospital Organization, 840, Murodo-cho, Izumi, Osaka 594-1101, Japan

[2]Institute for Frontier Life and Medical Sciences, Kyoto University, 53 Kawahara-cho, Shogoin, Sakyo-ku, Kyoto 606-8507, Japan

[3]INSERM UMR_S1109, Université de Strasbourg, Fédération de Médecine Translationnelle de Strasbourg (FMTS), Strasbourg 67000, France

[4]Present address: Department of Veterinary Anatomy, The University of Tokyo, Tokyo 113-8657, Japan

[5]Lead Contact

*Correspondence: imatsuo@wch.opho.jp

https://doi.org/10.1016/j.celrep.2020.107637

SUMMARY

Mammalian embryogenesis proceeds *in utero* with the support of nutrients and gases from maternal tissues. However, the contribution of the mechanical environment provided by the uterus to embryogenesis remains unaddressed. Notably, how intrauterine pressures are produced, accurately adjusted, and exerted on embryos are completely unknown. Here, we find that Reichert's membrane, a specialized basement membrane that wraps around the implanted mouse embryo, plays a crucial role as a shock absorber to protect embryos from intrauterine pressures. Notably, intrauterine pressures are produced by uterine smooth muscle contractions, showing the highest and most frequent periodic peaks just after implantation. Mechanistically, such pressures are adjusted within the sealed space between the embryo and uterus created by Reichert's membrane and are involved in egg-cylinder morphogenesis as an important biomechanical environment *in utero*. Thus, we propose the buffer space sealed by Reichert's membrane cushions and disperses intrauterine pressures exerted on embryos for egg-cylinder morphogenesis.

INTRODUCTION

Embryogenesis of a placental mammal proceeds *in utero* with the support of a nutrient supply and gas exchange between maternal tissues and the developing embryo. In fact, recent advances in *ex utero* culture of mouse embryos demonstrate embryo-autonomous development of mammalian early embryogenesis (Hsu, 1973; Bedzhov et al., 2014; Takaoka et al., 2017). Additional *in vitro* reconstituted models with pluripotent cells, such as gastruloids and organoids, further support embryo-autonomous mechanisms of mammalian development (Eiraku et al., 2011; Beccari et al., 2018; Bedzhov and Zernicka-Goetz, 2014). However, since the orderly development of implanted embryos in *ex utero* culture in time and space is still challenging (Vianello and Lutolf, 2019), non-embryo-autonomous mechanisms may be involved in early mouse embryogenesis in parallel with self-organization mechanisms. Accordingly, it seems likely that crucial unknown factors are present in uterine environments for normal development, with the exception of a nutrient supply and gas exchange.

Vertebrate eggs and early embryos are initially covered by acellular egg envelopes secreted by maternal tissues to protect from the hazardous external environment (Dumont and Brummett, 1985). In particular, the eggs of a placental mammal are initially covered with an acellular egg envelope called the zona pellucida. Subsequently, embryos hatch from the zona pellucida to be implanted into the uterus at the late blastocyst stage. Immediately after implantation, they are then surrounded by extraembryonic membranes, known as Reichert's membrane (RM), which separates the embryo proper from uterine tissues in rodents (Salamat et al., 1995; Hogan et al., 1980, 1984; Leivo et al., 1980; Smith and Strickland, 1981). RM, a specialized basement membrane (BM) composed of extracellular matrix (ECM) including laminin, collagen type IV (COL IV), and nidogen, is secreted from embryonic cells (Salamat et al., 1995; Hogan et al., 1980, 1984; Leivo et al., 1980; Smith and Strickland, 1981). RM is the only structure to enclose the embryo until the amnion develops and wraps the embryo proper at the typical inverting of the mouse embryo from an egg-cylinder shape. After that, RM collapses when the placenta is completely established. Therefore, RM is thought to serve as a permeable filter to allow the diffusion of gases and nutrients through a liquid-like amniotic fluid between the embryo and maternal tissues until the placental tissues are formed (Jollie, 1968). Over the past decade, it has become obvious that the mechanical properties of the ECM play important roles not only in cellular behaviors such as proliferation, migration, and differentiation but also in dynamic morphological changes during early embryogenesis (Charras and Sahai, 2014; Ladoux and Mège, 2017; Vining and Mooney,

2017). However, little attention has been paid to the role of RM in early mammalian development.

Mouse embryos morphologically change from the spherical shape of preimplanted blastocysts to the elongated egg-cylinder shape of post-implanted embryos during peri-implantation stages (Copp, 1979; Smith, 1985). The egg-cylinder shape is typical of rodent embryos and thought to be beneficial for multiple pregnancies. This morphological change is closely linked to proximal-distal (P-D) axis polarization (Beddington and Robertson, 1999; Mesnard et al., 2006; Matsuo and Hiramatsu, 2017), i.e., the formation of distal visceral endoderm (DVE); DVE cells then migrate to the prospective anterior side to establish an anterior-posterior (A-P) axis (Beddington and Robertson, 1999; Thomas and Beddington, 1996; Thomas et al., 1998; Srinivas et al., 2004). With respect to biochemical signaling, extra-embryonic ectoderm and proximal epiblast regions are considered to function as active sources of posteriorizing (caudalizing) signals, such as bone morphogenetic factors, Wnt, and members of the transforming growth factor-β family, to develop the posterior region of the body, while DVE cells, which express antagonists of the above ligands, such as *Cer1* and *lefty*, can suppress posteriorizing signals to develop the anterior region of the body (Beddington and Robertson, 1999; Kimura et al., 2000; Mesnard et al., 2006; Niehrs 2010; Stern and Downs, 2012; Bier and De Robertis, 2015). Additionally, as for the biomechanical aspect of the developing embryo, we have previously shown that physical confinement of early mouse embryos, mimicking the uterine environment, is crucial to elongation into an egg-cylinder shape. Elongation of the egg-cylinder shape itself maximizes the bending moment exerted on the distal tip of the implanted embryo and, thereby, DVE is induced through a local breach of the BM between the epiblast and visceral endoderm (VE) (Matsuo and Hiramatsu, 2017; Hiramatsu et al., 2013). However, the mechanical environment provided by the uterus, which controls early morphogenesis, has not yet been investigated (Vianello and Lutolf, 2019; Matsuo and Hiramatsu, 2017). Notably, we have very limited information on how substantial intrauterine mechanical pressures are produced and accurately adjusted in early mouse embryos and how these mechanical factors contribute to early mouse morphogenesis in utero. Given that the change in embryonic shape, from a spherical blastocyst into an elongated egg-cylinder, coincides with the replacement of embryo-wrapping architectures from the zona pellucida to RM upon implantation, it can be hypothesized that RM may play a mechanical role in egg-cylinder morphogenesis.

Here, we reveal that RM-defective mouse embryos display a deformed embryonic shape during egg-cylinder morphogenesis. With respect to mechanical factors in the uterus for early mouse embryogenesis, we show that uterine muscle contractions produce high and periodic intrauterine pressures at peri-implantation stages. These high mechanical pressures are cushioned and dispersed by the sealed buffer space between embryos and uterus created by RM and, thereby, are accurately exerted on early implanted embryos necessary for egg-cylinder morphogenesis.

RESULTS

RM Is Necessary for Egg-Cylinder Morphogenesis

To assess the role of RM in early morphogenesis, we analyzed laminin subunit α1 (*Lama1*) homozygous mutant (*Lama1*$^{-/-}$) embryos in which RM was considered to be lost (Alpy et al., 2005). Since *Lama1*$^{-/-}$ embryos appeared to be absorbed and died until embryonic day 7.5 (E7.5) (Figures S1A and S1B; Table S1), we compared their morphology and ECM protein expression, which consisted of RM, between wild-type and *Lama1*$^{-/-}$ embryos at E5.5 and E6.5 (Figures 1A–1D). In wild-type embryos, their morphology was a smooth egg-cylindrical shape during these periods (Figures 1A and 1B; white dashed lines). Accordingly, the components of the RM, laminin subunit α1 (LAMA1), and COL IV proteins, were heavily deposited throughout the RM at E5.5 and E6.5 (Figures 1A and 1B; arrowheads). Conversely, in *Lama1*$^{-/-}$ embryos, LAMA1 was undetectable in any embryonic structures except maternal tissues, while COL IV was detected in the BM of the VE side (Figures 1C and 1D; arrows), but not in the border between the embryo and decidua corresponding to RM (Figures 1C and 1D). These findings indicated that a RM structure was not formed in *Lama1*$^{-/-}$ embryos. To further verify if the basal lamina structure of RM was absent in *Lama1*$^{-/-}$ embryos, we examined these by transmission electron microscopy (Figures 1E–1H). In E6.5 wild-type embryos, the basal lamina structure, several hundred nanometers in thickness, was evident between parietal endoderm (PaE) and trophoblast giant (TBG) cells (Figures 1E and 1F, an asterisk). However, in *Lama1*$^{-/-}$ embryos, such a basal lamina structure was not detectable (Figures 1G and 1H). Therefore, TBG and VE cells appeared to adjoin each other (Figure 1G). These results clearly demonstrate that *Lama1*$^{-/-}$ embryos fail to form RM at the ultrastructural level.

More strikingly, *Lama1*$^{-/-}$ embryos displayed apparently normal morphology at E5.5 (Figure 1C, dashed line) but severe deformation of the embryonic shape later at E6.5 (Figure 1D, dashed line). Such deformed features in *Lama1*$^{-/-}$ E6.5 embryos included a distorted epiblast and extraembryonic ectoderm (Figures 1I–1K). To evaluate the severity of deformed embryonic shapes quantitatively, we measured the degree of shifted slopes between the rectilinear and actual center lines of the embryo and compared the degrees of angular differences between wild-type and *Lama1*$^{-/-}$ embryos (Figure 1L). We found that angular differences of *Lama1*$^{-/-}$ embryos were much larger than those of the wild type at E6.5 (Figure 1M).

To further analyze whether the deformation of *Lama1*$^{-/-}$ embryos is involved in their embryonic and cellular abnormalities, such as cell fate specification, cell proliferation, and apoptosis, we examined several specific markers (Figures S1C–S1N). The expression of *Bmp4*, *Cdx2*, *Hex*, and *Oct4* transcripts, markers for extraembryonic ectoderm, DVE, and epiblast, respectively, at E5.5, was detected at appropriate regions similar to those of wild-type embryos (Figures S1C–S1J). Thus, the fate of these three tissue layers of *Lama1*$^{-/-}$ embryos was normally specified. Additionally, there was no difference in the expression of cell proliferation and apoptosis markers between wild-type and *Lama1*$^{-/-}$ embryos at E5.5 (Figures S1K–S1N), although apoptotic cells were increased later at E6.5 in *Lama1*$^{-/-}$ embryos

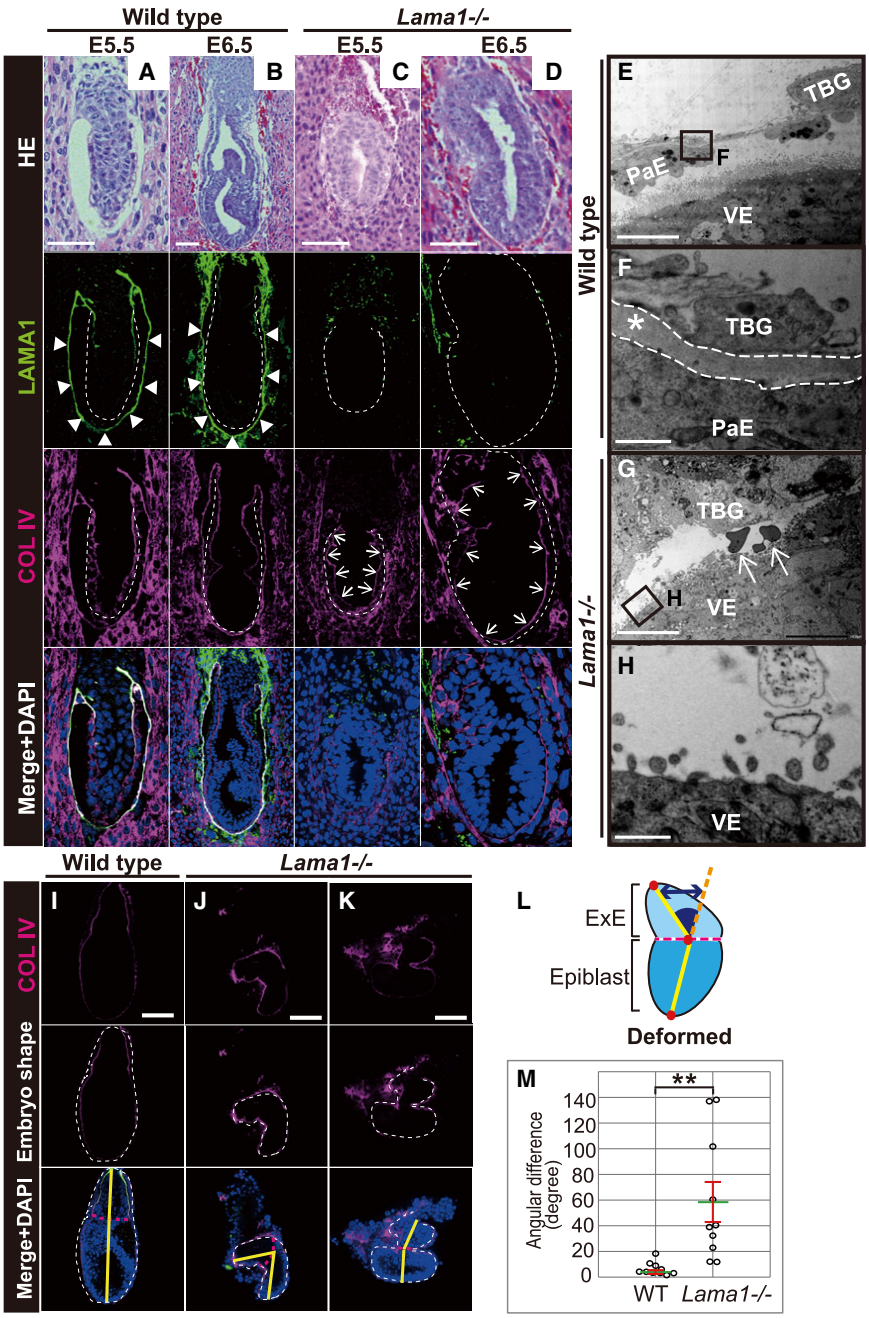

Figure 1. Morphological Abnormalities in *Lama1*$^{-/-}$ Embryos at E5.5 and E6.5

(A–D) Histological and immunohistochemical analyses in wild-type (A and B) and *Lama1*$^{-/-}$ (C and D) embryos with decidua at E5.5 (A and C) and E6.5 (B and D). Laminin subunit α1 (LAMA1; green), collagen type IV (COL IV; magenta), and nuclei (DAPI, blue) are shown. Embryonic regions are enclosed in an egg-cylinder shape by white dashed lines. Reichert's membrane (RM) is indicated by white arrowheads shown in green in LAMA1 panels and also shown in white in merged panels by green (LAMA1) and magenta (COL IV) colors (A and B). Neither LAMA1 (green) nor COL IV (magenta) was detected at the basement membrane (BM) between the embryo and decidua tissue in *Lama1*$^{-/-}$ embryos (C and D). COL IV expression between the visceral endoderm (VE) and epiblast was detected (C and D, arrows). The egg-cylinder shape of the *Lama1*$^{-/-}$ embryo was deformed at E6.5, as indicated by white dashed lines.

(E–H) Transmission electron micrographs of wild-type (E and F) and *Lama1*$^{-/-}$ embryos (G and H) at E6.5. n = 2 (wild-type), 4 (*Lama1*$^{-/-}$) embryos. Solid-boxed areas in (E) and (G) are highly magnified (F and H). RM (asterisk) is only detected between trophoblast giant (TBG) cells and parietal endoderm (PaE) cells in the wild type (F). Maternally derived red blood cells are present between the VE and TBG cells of the *Lama1*$^{-/-}$ embryo (arrows) (G).

(I–K) Immunohistochemistry of COL IV (magenta) with nuclei (DAPI, blue) in wild-type (I) and *Lama1*$^{-/-}$ (J and K) embryos at E6.5. White dashed lines indicate embryonic shapes. Yellow polygonal lines connect three points (the most distal center, the center of the boundary between the epiblast and extraembryonic ectoderm [magenta dashed lines], and the most proximal center), corresponding to the normal or deformed shape of embryos.

(L) A schematic image of a deformed embryo. The yellow lines connect three red points as in (I)–(K). Deformed shapes are quantified to measure angular differences between the lines connecting two points. Total values of two angular differences are calculated.

(M) Degrees of angular differences of wild-type and *Lama1*$^{-/-}$ embryos at E6.5. Green lines indicate the mean value, and red lines represent standard error (SE) bars (two-tailed *U* test, **p < 0.01). n = 10 (wild-type), 10 (*Lama1*$^{-/-}$) embryos. Scale bars represent 50 μm (A–D), 10 μm (E and G), 1 μm (F and H), and 100 μm (I–K). Images are representative of analyzed embryos (Table S6). See also Figure S1 and Table S1.

when mutant embryos were already deformed (Alpy et al., 2005). These findings support the idea that the deformation of *Lama1*$^{-/-}$ embryos is not due to their cell fate, proliferation, and apoptosis but rather to the absence of RM. Consistent with this, conditional knockout embryos of the *Lama1* gene in epiblast-derived regions are able to develop until birth (Edwards et al., 2010; Ichikawa-Tomikawa et al., 2012). Together, these aforementioned results strongly suggest that RM is essential for correct morphogenesis, especially egg-cylinder shape formation, during E5.5 to E6.5.

To evaluate the relevance of RM formation to egg-cylinder morphogenesis more precisely, we accurately described developmental profiles of mouse RM at peri-implantation stages and found that RM formation appeared to be a prerequisite for egg-cylinder morphogenesis (Figure 2). Since LAMA1 and COL IV proteins are considered to be initially secreted and then deposited in the BM, we investigated their expression in late blastocysts just implanted at E4.5 (Figures 2A–2D). LAMA1 protein was localized throughout the BM, including the distal portion of the mural trophectoderm

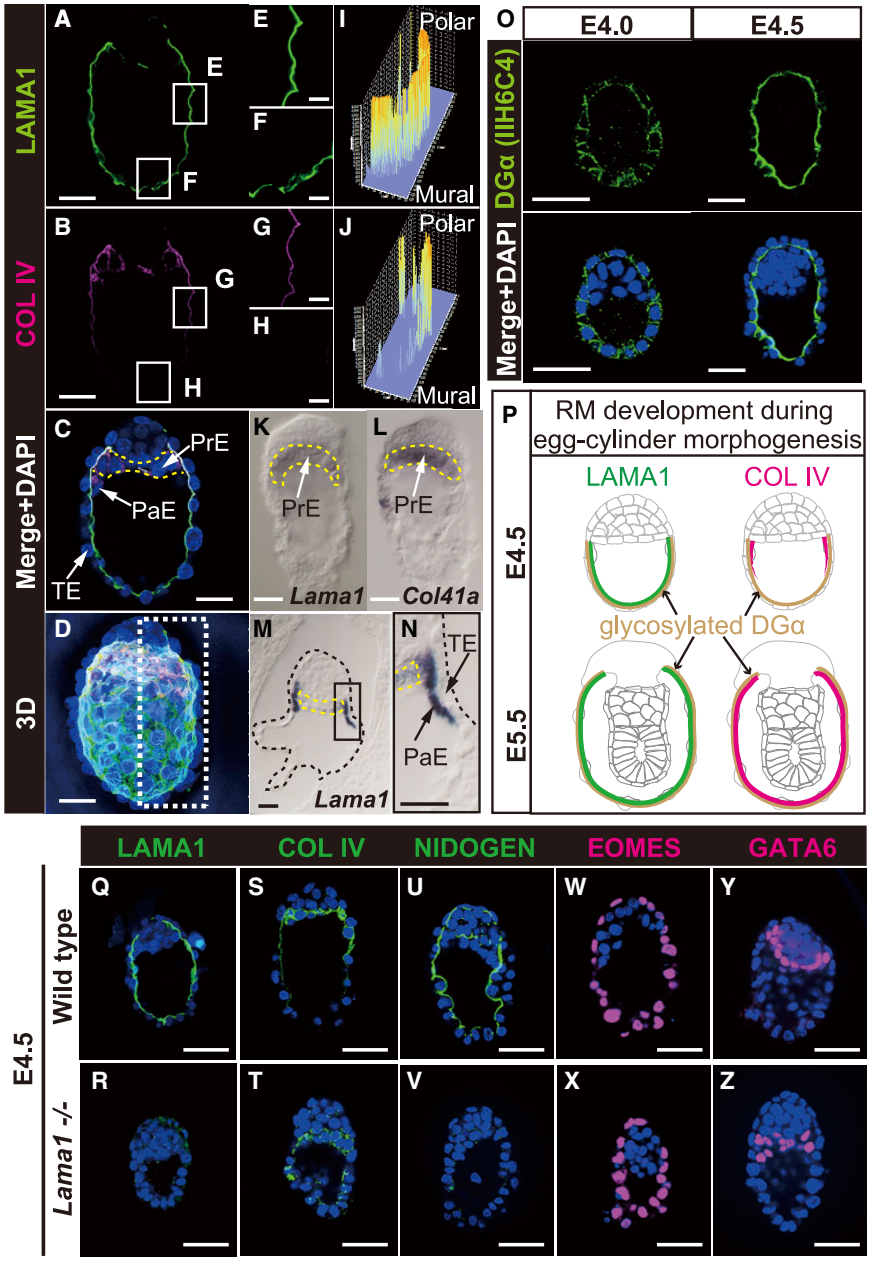

Figure 2. Developmental Profiles of RM at Peri-implantation Stages

(A–D) Immunohistochemistry of laminin subunit α1 (LAMA1, green) (A), COL IV (magenta) (B), merged with nuclei (DAPI, blue) (C), and their three-dimensional (3D) images (D) in a whole-mount wild-type embryo at E4.5.

(E–H) Higher magnifications of the areas with LAMA1 (green) and COL IV (magenta) in (A) and (B).

(I and J) Intensity of confocal 3D images obtained by LAMA1 (I) and COL IV (J) immunohistochemical analysis in (D).

(K and L) Whole-mount *in situ* hybridization of *Lama1* (K) and *Col41a* (L) mRNA in E4.5 embryos. Dashed yellow lines enclose a primitive endoderm (PrE) region.

(M) *In situ* hybridization of *Lama1* mRNA in paraffin-sectioned E4.5 embryos. The dashed black line shows the shape of the embryo in utero.

(N) The highly magnified boxed area in (M).

(O) Immunohistochemistry of glycosylated dystroglycan α (DGα [IIH6C4]; green), a crucial domain for a laminin anchor, and merged with nuclei (DAPI, blue) at E4.0 and E4.5.

(P) A schematic illustration of developmental profiles of RM in wild-type embryos. LAMA1 protein (green), glycosylated DGα (brown), and COL IV protein (magenta).

(Q–Z) Immunohistochemistry of extracellular matrix (ECM) proteins and cell-specific markers in wild-type (Q, S, U, W, and Y) and *Lama1*$^{-/-}$ (R, T, V, X, and Z) embryos at E4.5, including LAMA1 (Q and R), COL IV (S and T), and NIDOGEN (U and V). In *Lama1*$^{-/-}$ embryos, the ECM markers COL IV and NIDOGEN were not deposited properly in RM (T and V). Eomesodermin (EOMES) (W and X), expressed in trophectoderm (TE) cells, and GATA6 (Y and Z), expressed in PrE cells, are detected in both wild-type and *Lama1*$^{-/-}$ embryos.

Scale bars represent 25 μm (A–H, M, and N), 30 μm (K and L), and 50 μm in (O and Q–Z). Images are representative of analyzed embryos (Table S6).

(TE; Figures 2A, 2C–2F, and 2I). In comparison, COL IV was mainly expressed in the cytoplasm of primitive endoderm (PrE) cells and deposited mainly in the proximal, but not distal, portion of the mural TE (Figures 2B–2D, 2G, 2H, and 2J). Further mRNA expression studies indicated that the *Lama1* gene was expressed in PrE and PaE, while the α1 subunit of the COL IV (*Col41a*) gene was in PrE; both were not in the mural TE (Figures 2K–2N). However, their protein products were considered to be secreted and diffused in the extracellular space and, consequently, deposited in the BM of the TE. Consistently, a glycosylated form of α-dystroglycan, which anchors laminin as a membrane receptor, was distributed throughout the basal side of TE cells (Figure 2O). Additionally, COL IV expression has been shown to be dispensable for early embryogenesis (Pöschl et al., 2004). These aforementioned observations together demonstrated that RM formation commenced as the BM of mural TE cells and completed by elongating stage at E5.5 through the initial deposition of LAMA1, which was anchored partly by α-dystroglycan at E4.5 prior to egg-cylinder morphogenesis (Figure 2P).

To verify whether *Lama1*$^{-/-}$ embryos fail to form RM when the egg-cylinder elongates, the initial deposition of the BM was analyzed (Figures 2Q–2Z). In agreement with our assumption, in *Lama1*$^{-/-}$ embryos, ECM proteins, LAMA1, COL IV, and NIDOGEN were not deposited properly at E4.5 (Figures 2Q–2V), while expression of eomesodermin (EOMES) and GATA6, specific markers for the extraembryonic regions, TE, PrE, and PaE, appeared to be normally localized (Figures 2W–2Z). These findings indicated that PrE and PaE cells, which

produce ECM components for RM, were able to be specified without *Lama1*; however, the RM structure itself was absent in *Lama1*$^{-/-}$ embryos from the very beginning. These results indicate that a loss of ECM protein deposition at E4.5 is evident in the prospective RM prior to egg-cylinder morphogenesis in *Lama1*$^{-/-}$ embryos. Taken together, these developmental profiles of RM strongly suggest that RM may contribute to egg-cylinder morphogenesis.

RM Creates Space between Embryo and Decidua

To explore how RM is associated with egg-cylinder morphogenesis more precisely, we investigated the blank space between the embryo and decidua from E5.5 to E6.5 that was suggested to be present according to a histological sectional view at E5.5 (Figure 1A). To quantitatively visualize three-dimensional (3D) images of the space and avoid shrinkage of the morphology due to fixing and sectioning procedures, we exploited high-resolution micro-computed tomography (micro-CT) analysis, a nondestructive and noninvasive technique, for E5.5 and E6.5 embryos (Figures 3A–3J). At E5.5, the lateral blank space between the VE and decidua was present at the level of the extraembryonic ectoderm as well as at the level of the epiblast (Figures 3D and 3E, black). At the subsequent E6.5, the lateral space between the VE and decidua was undetectable, including at the level of the epiblast (Figures 3I and 3J). These results indicated that a blank space between the embryo and decidua, which was larger than the total embryo volume (Table S2), was present at E5.5 but that the space was greatly reduced at E6.5. Taken together with 3D image analysis, these results suggest that RM functions not only to separate the embryo from maternal tissues but also to provide space between the embryo and decidua during early implantation stages.

To investigate whether RM is actually involved in the generation of the blank space, we next similarly analyzed *Lama1*$^{-/-}$ embryos with micro-CT (Figures 3K–3T). Consequently, we found that the blank space between the embryo and decidua was completely lost throughout *Lama1*$^{-/-}$ embryos at E5.5 as well as E6.5 (Figures 3K–3T). These findings demonstrate that RM is essential for the formation of the blank space between the embryo and decidua during early implantation stages.

Space Created by RM Protects Embryonic Shape

Given that the blank space between the embryo and decidua is created by RM during egg-cylinder morphogenesis, we hypothesized that RM may be necessary for correct egg-cylinder morphogenesis by generating the blank space in utero. To explore if this mechanism is likely to be involved, we exploited Fukutin (*Fktn*) mutant embryos in which RM was considered to exhibit hypoplasia (Kurahashi et al., 2005). Consequently, *Fktn*$^{-/-}$embryos appeared to be degenerated or severely retarded by E8.5 (Figures S2A–S2C; Table S3). *Fktn*, encoding a glycosyltransferase, is involved in the biosynthesis of the glycosylated form of α-dystroglycan, which is crucial to anchor laminin in a BM.

To observe whether the *Fktn*$^{-/-}$ embryo was tightly sealed by RM to create space, we analyzed *Fktn*$^{-/-}$ RM histologically (Figures 4A–4D and S2D–S2H). In wild-type embryos, the glycosylated form of α-dystroglycan was detected in trophoblastic cells, and RM was deposited with COL IV (Figure 4A). Conversely, in *Fktn*$^{-/-}$ embryos, glycosylated α-dystroglycan-positive cells were poorly represented (Figure 4B). Visualization of 3D reconstructed images and confocal images of COL IV expression revealed that RM contained holes and was torn in *Fktn*$^{-/-}$ embryos (Figures 4C and 4D, white arrows and arrowheads; Figures S2E and S2F). Importantly, deformation of the embryonic shape was detected in *Fktn*$^{-/-}$ embryos, but not in wild-type embryos, at E6.5 (Figures 4B, 4E, and S2H). To further quantitatively visualize the space between the embryo and decidua, we analyzed *Fktn*$^{-/-}$ embryos by micro-CT. Consequently, the blank space between the embryo and decidua was completely lost in *Fktn*$^{-/-}$ embryos at E5.5, similar to that observed in *Lama1*$^{-/-}$ embryos (Figures 4F–4J).

To exclude the possibility of the deformed shape of *Fktn*$^{-/-}$ embryos being involved in abnormalities of cell fate specification, we examined the expression of *Bmp4*, *Cdx2*, *Hex*, and *Oct4* transcripts, markers for extraembryonic ectoderm, DVE, and epiblasts, respectively, at E5.5 (Figures S3A–S3H). Transcripts of these genes were detected in normal positions; thus, fate specification of these three tissue layers in *Fktn*$^{-/-}$ embryos was likely normal (Figures S3A–S3H). Additionally, there was no apparent difference in terms of the expression of cell proliferation and apoptosis markers between wild-type and *Fktn*$^{-/-}$ embryos (Figures S3I–S3L). These results show that the deformation of *Fktn*$^{-/-}$ embryos cannot be attributed to abnormalities in embryo-autonomous development, such as proliferation and apoptosis, like in *Lama1*$^{-/-}$ embryos as described above. Consistent with these results, epiblast-specific functional mutations of the *Fktn* gene do not affect early embryogenesis in mice (Beedle et al., 2012; Whitmore et al., 2014). Taken together, these aforementioned findings suggest that the completely sealed blank space created by RM may be necessary for egg-cylinder morphogenesis.

Smooth Muscle Contractions Exert High and Periodic Intrauterine Pressures on Embryos

In the uterus, mouse embryos are surrounded by decidual tissues, with the most outer side covered with myometrium consisting of uterine smooth muscle (Figures 5A–5C). Previously, we have shown that physical confinement mimicking the uterine environment is crucial to elongation into an egg-cylinder shape (Hiramatsu et al., 2013). Although uterine smooth muscle exerts intrauterine pressures, otherwise known as labor, at delivery in the late stage of a mouse pregnancy (Pierce et al., 2010; Grotegut et al., 2016; Rada et al., 2015; Robuck et al., 2018), its effects during early implantation stages remain unexplored. To address how much mechanical stress is exerted on embryos *in utero*, we directly measured intrauterine pressures at peri-implantation stages by inserting a microtransducer-mounted catheter into intrauterine space through one side of exposed uterine horn (Figure 5D). We found that intrauterine pressures of non-pregnant uteri were periodically detected due to smooth muscle contraction and relaxation (Figure 5E, NP). Intrauterine pressure curves were evaluated with amplitude, an average contractile integral (AUC), frequency, duration and Montevideo units, following previously described methods (Robuck et al., 2018) (Figure 5F). After fertilization from E3.5 to E6.5, the amplitude, AUC, frequency, and Montevideo units were increased compared with those of

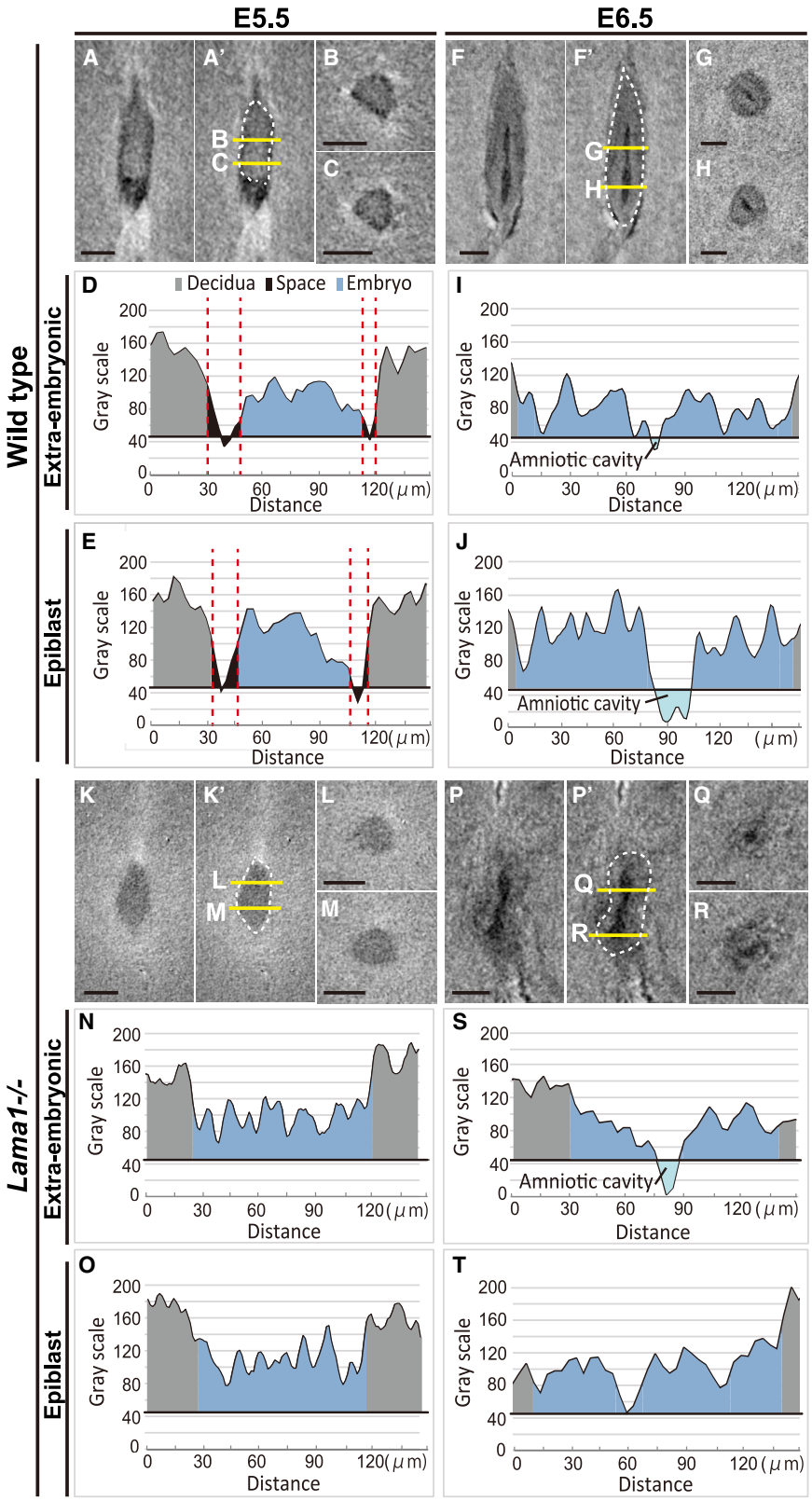

Figure 3. Quantification of the Space between the Embryo and Decidua with Micro-computed Tomography

(A–C) Representative sagittal (A and A′) and transverse views (B and C) of a wild-type embryo and decidua with micro-computed tomography (CT) at E5.5. n = 5.

(D and E) Profile data of gray levels were obtained along each yellow line (B and C) through the embryos (white dashed lines) shown in (A′). The lines indicate signal intensity images at the level of the extraembryonic ectoderm (D and B in A') and epiblast (E and C in A'). Blank space (painted black) is present at both levels.

(F–H) Representative sagittal (F and F′) and transverse views (G and H) of a wild-type embryo and decidua with micro-CT at E6.5. n = 8.

(I and J) Profile data of gray levels were obtained along each yellow line (G and H) through the embryos (white dashed lines) shown in (F′). The lines indicate signal intensity images at the level of the extraembryonic ectoderm (I and G in F') and epiblast (J and H in F'). Blank space (painted black) is not present at extraembryonic ectoderm or epiblast levels.

(K–M) Representative sagittal (K and K′) and transverse views (L and M) of a *Lama1*$^{-/-}$ embryo and *Lama1*$^{+/-}$ decidua with micro-CT at E5.5. n = 3.

(N and O) Profile data of gray levels were obtained along each yellow line through the embryos (white dashed lines) shown in (K′). The lines indicate signal intensity images at the level of the extraembryonic ectoderm (N and L in K') and epiblast (O and M in K').

(P–R) Representative sagittal (P and P′) and transverse views (Q and R) of a *Lama1*$^{-/-}$ embryo and *Lama1*$^{+/-}$ decidua with micro-CT at E6.5. n = 4.

(S and T) Profile data of gray levels were obtained along each yellow line (Q and R) through the embryos (white dashed lines) shown in (P′). The lines indicate signal intensity images at the level of the extraembryonic ectoderm (S and Q in P') and epiblast (T and R in P').

The spaces without cells are judged as a gray level under 45. Scale bars, 100 μm (A–C, F–H, K–M, and P–R). See also Table S2.

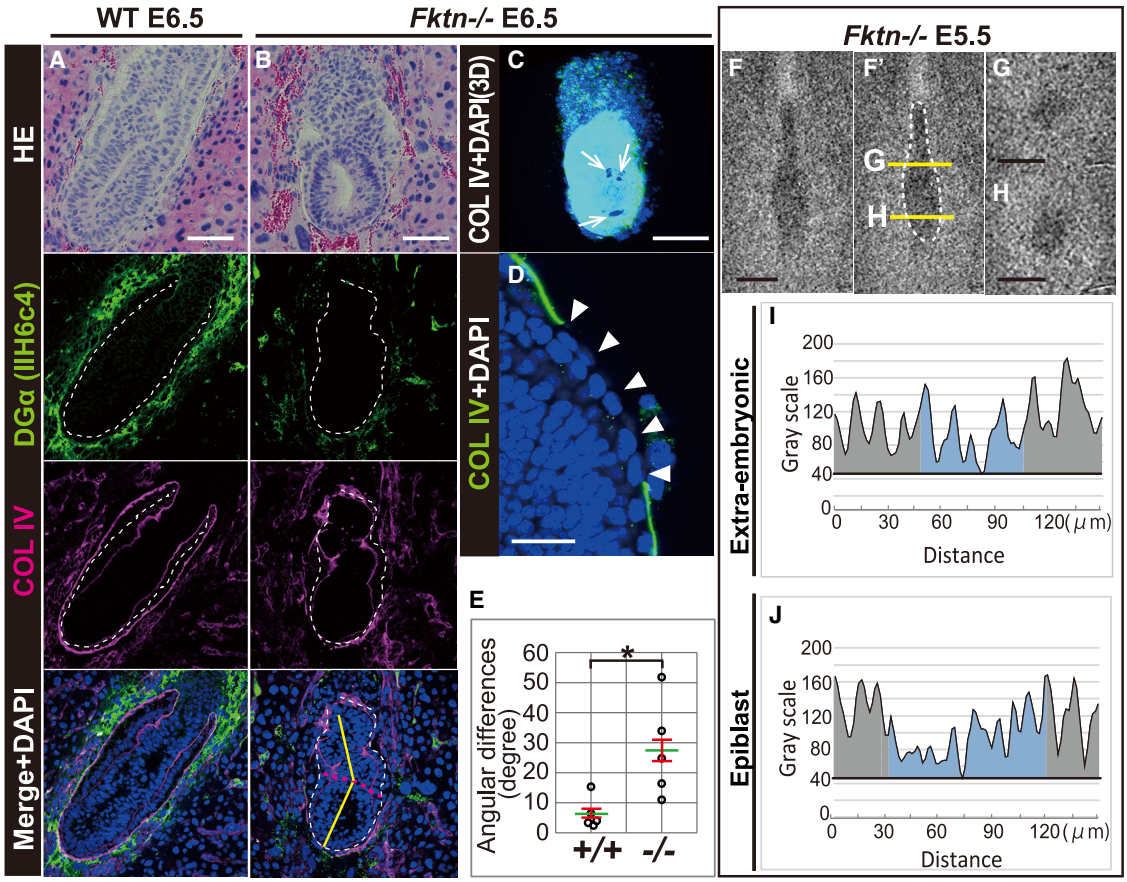

Figure 4. The Sealed Space Constructed by RM Is Absent in *Fktn*$^{-/-}$ Embryos

(A and B) Histological and immunohistochemical analyses using paraffin sections in wild-type (A) and *Fktn*$^{-/-}$ (B) embryos, together with maternal decidua at E6.5. Glycosylated dystroglycan α (DGα [IIH6C4]; green) bound to laminin, COL IV (magenta), and nuclei (DAPI, blue) are shown. Embryonic regions are enclosed by white dashed lines. DGα [IIH6C4] expression is diminished in the *Fktn*$^{-/-}$ embryo (B, green).

(C) A 3D image shows that RM has holes (white arrows) after whole-mount immunohistochemistry of COL IV (green) merged with nuclei (DAPI, blue) in *Fktn*$^{-/-}$ embryos.

(D) Sectional views of a discontinuous RM (white arrowheads) with immunohistochemistry of COL IV (green) merged with nuclei (DAPI, blue).

(E) Degree of angular differences of wild-type (+/+) and *Fktn*$^{-/-}$ (−/−) embryos at E6.5. Green lines indicate the mean value and red lines represent the standard error (SE; two-tailed *U* test, *p < 0.05). n = 5 (+/+) and 5 (−/−) embryos.

(F–H) Micro-computed tomography (CT) representative sagittal (F and F′) and transverse views (G and H) of the *Fktn*$^{-/-}$ embryo and *Fktn*$^{+/-}$ decidua at E5.5 (n = 3).

(I and J) Profile data of gray levels were obtained along each yellow line (G and H) through the embryos (white dashed lines) shown in (F′). The lines indicate signal intensity images at the level of the extraembryonic ectoderm (I and G in F') and epiblast (J and H in F'). The spaces without cells are judged as a gray level under 45. Scale bars represent 100 μm (A–C); 12.5 μm in (D); 100 μm in (F–H). Images are representative of analyzed embryos (Table S6). See also Figures S2 and S3 and Table S3.

non-pregnant uteri (Figures 5E and 5F). Strikingly, the amplitude was greatly increased to a high of 60.67 ± 2.44 mmHg at E5.5 as compared with a high of 42.46 ± 1.26 mmHg at E3.5 (Figures 5E–5G); however, it subsequently decreased to 43.83 ± 2.68 mmHg at E6.5 (Figures 5E–5G). The AUC, frequency, and Montevideo units also became higher in E5.5 uteri than in E3.5 and E6.5 uteri (Figure 5F). These findings revealed that intrauterine pressures were highest and most frequent at E5.5 during peri-implantation stages.

To exclude the possibility that our approach in measuring intrauterine pressures within decidua disrupts normal values, we also examined intrauterine pressures in a relatively noninvasive transcervical manner (Figures S4A and S4B; Robuck et al., 2018). We compared the amplitude measured with an abdominal operation through an exposed uterine horn to that with a transcervical protocol through the vagina at E6.5 and found that these two amplitudes did not significantly differ (Figures S4A–S4C). In addition, to test whether these measurements affected the viability of mother and offspring, we fostered these mothers for a further several days after the measurement. Consequently, we found that such treated mothers survived the operation and their offspring were delivered normally (Figures S4D and S4E). These additional data support the feasibility of measuring the above intrauterine pressures using our protocol.

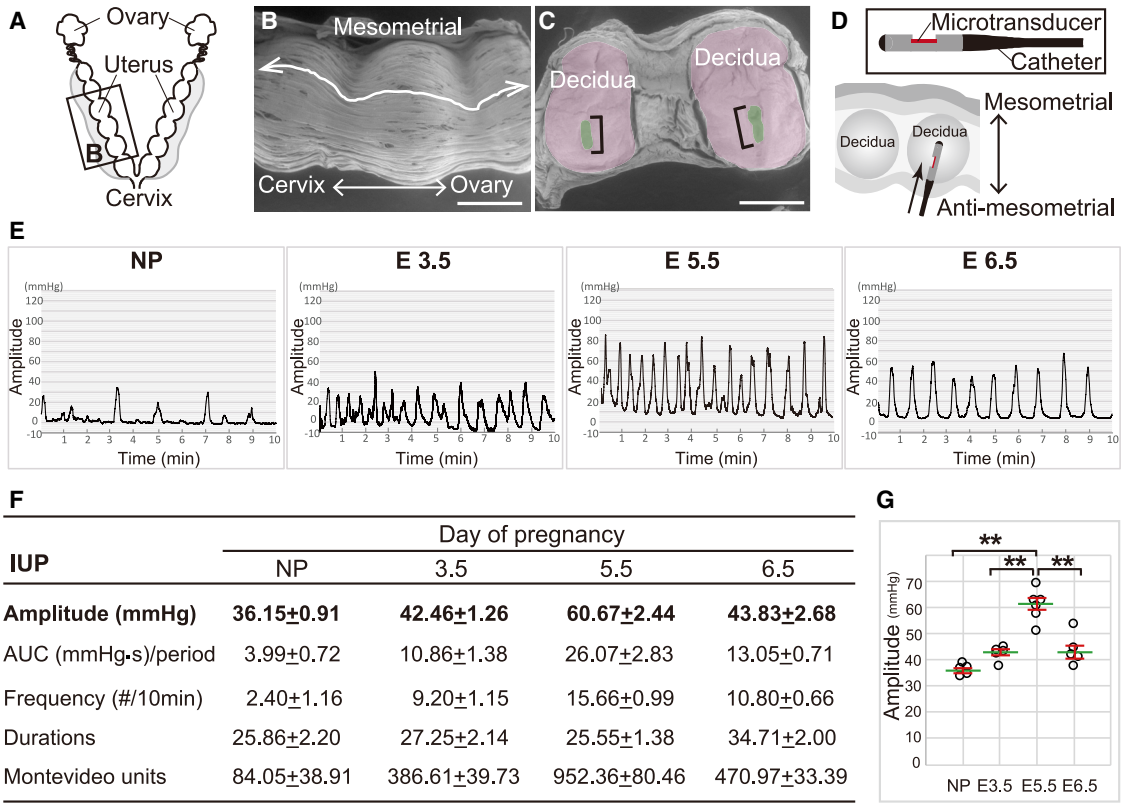

F

IUP	Day of pregnancy			
	NP	3.5	5.5	6.5
Amplitude (mmHg)	**36.15±0.91**	**42.46±1.26**	**60.67±2.44**	**43.83±2.68**
AUC (mmHg•s)/period	3.99±0.72	10.86±1.38	26.07±2.83	13.05±0.71
Frequency (#/10min)	2.40±1.16	9.20±1.15	15.66±0.99	10.80±0.66
Durations	25.86±2.20	27.25±2.14	25.55±1.38	34.71±2.00
Montevideo units	84.05±38.91	386.61±39.73	952.36±80.46	470.97±33.39

Figure 5. High and Periodic Intrauterine Pressures Are Exerted on Embryos during Early Pregnancy

(A) Schematic figure of reproductive organs in the female mouse.

(B and C) Scanning electron micrographs of a pregnant uterus covered with longitudinal uterine muscle fibers. Outlook (B) and sectional views (C) show deciduae in pink and embryos in green (indicated by brackets). n = 8.

(D) Schematic illustrations of a micro-transducer mounted catheter and its insertion point.

(E) Waveforms of intrauterine contractile pressures on non-pregnant (NP), E3.5, E5.5, and E6.5 uteri.

(F) Amplitude (namely, averages) of the intrauterine pressures, average contractile integral (AUC), frequency, duration, and Montevideo unit of NP, E3.5, E5.5, and E6.5 uteri for 10 min. ± indicates SE.

(G) Averages of amplitude in (F) are shown as a scatterplot for NP, E3.5, E5.5, and E6.5 uteri for 10 min. Green lines indicate the mean value, and red lines represent the SE (one-way ANOVA followed by Tukey-Kramer, **$p < 0.01$). n = 5 (NP), 5 (E3.5), 6 (E5.5), and 5 (E6.5) embryos. Scale bars, 1 mm (B and C). See also Figure S4.

Reduction of Intrauterine Pressures Can Complement the Deformed Embryonic Shape of RM-Deficient Embryos

To verify our hypothesis that deformation of *Lama1*$^{-/-}$ embryos lacking RM is caused by high and periodic intrauterine pressures, in particular at E5.5, we attempted to decrease intrauterine pressure. Prior to testing this assumption, we ruled out the possibility that the aberrant environment of a *Lama1* heterozygous mutant (*Lama1*$^{+/-}$) uterus might cause such a deformation in *Lama1*$^{-/-}$ embryos, though the morphology of the decidua of wild-type and *Lama1*$^{+/-}$ uteri did not differ (Figures 1A–1D). Therefore, intrauterine pressures of *Lama1*$^{+/-}$ mothers were measured using a microtransducer-mounted catheter (Figure S5A). Consequently, we found that the intrauterine pressures of *Lama1*$^{+/-}$ mothers were not significantly changed from those of wild-type mothers during peri-implantation stages (Figure S5B). In agreement with this result, fertilized oocytes intercrossing from *Lama1*$^{+/-}$ mice were transplanted into the wild-type mother uterus (Figure S5C). E6.5 *Lama1*$^{-/-}$ embryos fostered in a wild-type female displayed a deformed egg-cylinder shape almost comparable to that observed in the *Lama1*$^{+/-}$ uterus (Figures S5D–S5F). These findings definitively show that the deformed shape of *Lama1*$^{-/-}$ E6.5 embryos is not due to an aberrant *Lama1*$^{+/-}$ uterine environment.

We then examined if intrauterine pressures could be decreased by an activator of the β_2-adrenoreceptor, salbutamol, which relaxes uterine smooth muscles (Chen et al., 2011). When intrauterine pressures were measured after salbutamol administration, we found that these were significantly decreased (Figures 6A, 6B, and S6A). This result indicates that uterine smooth muscle contractility clearly contributes to the intrauterine pressure. To further analyze whether the administration of salbutamol has adverse effects on the implantation itself, we examined the expression of cyclooxygenase 2 (COX2) and the phosphorylated form of STAT3, markers for normal implantation in the uterus (Figures S6B–S6Q). No difference was observed between the

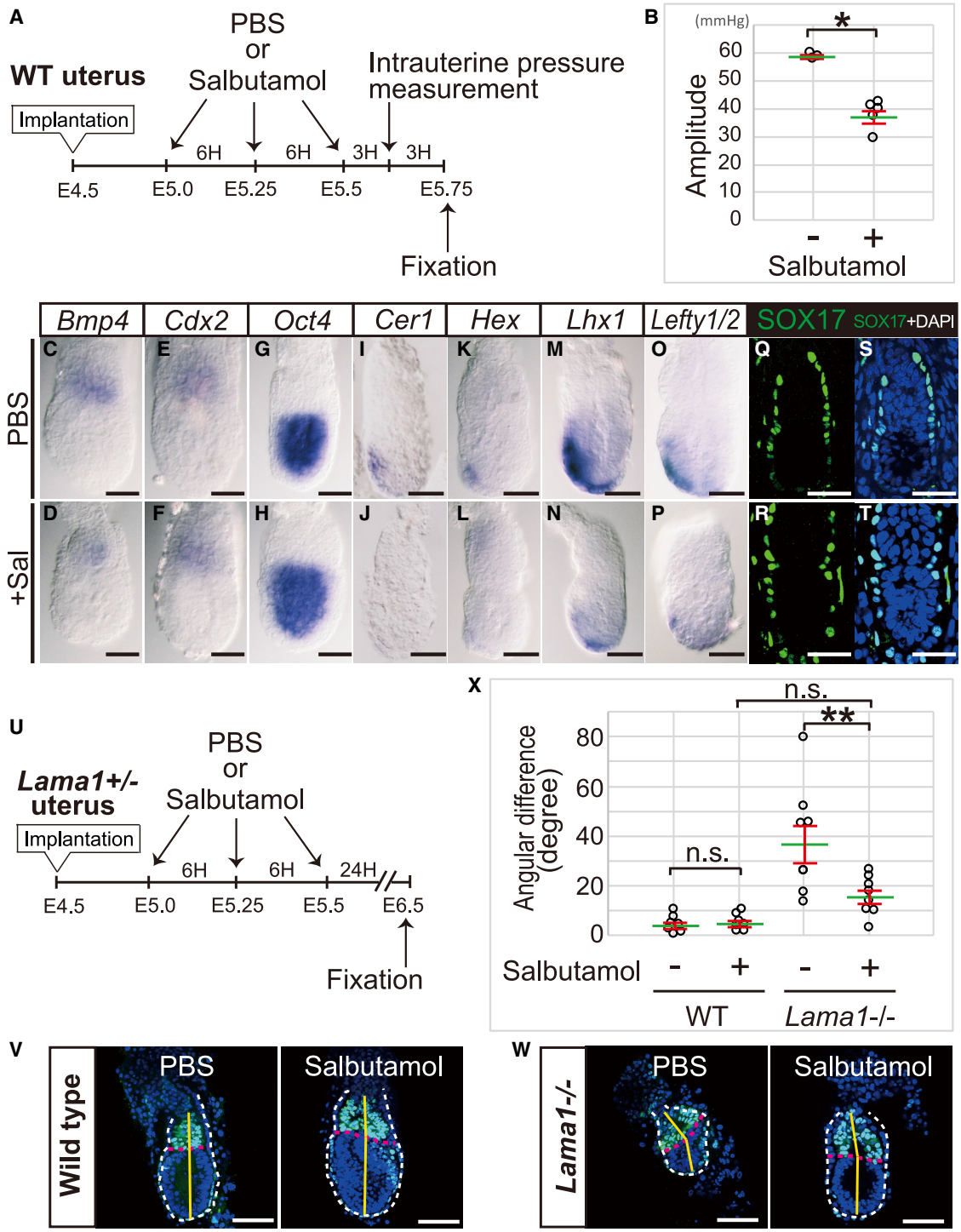

Figure 6. Reduction of Intrauterine Pressures Affects DVE Specification on Wild-Type Embryos and Can Rescue the Deformation of *Lama1*$^{-/-}$ Embryos

(A) A schematic schedule of the administration of salbutamol or phosphate-buffered saline (PBS) to wild-type mothers. Salbutamol or PBS (as a control) was administered three times every 6 h from E5.0 to E5.5, and then uterine pressures were measured and embryos were fixed at E5.75.

(B) Averages of the amplitudes of intrauterine pressures after treatment with only PBS without salbutamol (−; 59.01 ± 0.69 mmHg) or with salbutamol (+; 38.06 ± 2.27 mmHg). The amplitudes of intrauterine pressures in salbutamol-treated mothers are markedly decreased compared to those of PBS-treated mothers. Green lines indicate the mean value and red lines represent the standard error (SE). (two-tailed *U*-test, *p < 0.05). n = 4 (without salbutamol), n = 5 (with salbutamol) embryos.

(legend continued on next page)

salbutamol- and PBS-administered uterus at E5.5 (Figures S6B–S6Q). These results show that the administration of salbutamol has little adverse effect on implantation and the early pregnancy phase of the uterus.

Next, to further exclude whether the administration of salbutamol could result in the inappropriate cell fate specification of implanted embryos, we assessed the expression of the cell fate markers *Bmp4* and *Cdx2* for extraembryonic ectoderm, *Oct4* for epiblast, and SOX17 for the entire VE (Figures 6C–6H and 6Q–6T). Such cell fate markers were expressed in the appropriate tissue layers, indicating that extraembryonic ectoderm, epiblast, and VE were normally specified (Figures 6C–6H and 6Q–6T). With respect to DVE specification, we examined DVE-related markers and found that *Cer1* and *Hex* were not expressed, and *Lhx1* and *Lefty1/2* were not properly induced at E5.75 (Figures 6I–6P). These findings indicate that intrauterine pressures are necessary for proper DVE specification as an important biomechanical environment in utero, as previously proposed (Hiramatsu et al., 2013; Matsuo and Hiramatsu, 2017). However, at subsequent E6.5, salbutamol-treated embryos expressed *Cer1*, an AVE marker, and *T*, a primitive streak marker, at a normal position (Figures S6R–S6U). Additionally, at subsequent E9.5 and birth, they appeared to develop and be delivered normally (Tables S4 and S5). These aforementioned results demonstrate that both the uterus and embryos appear to proceed normally in the early pregnancy phase, even after salbutamol treatment, except for the timing of DVE specification (see Discussion).

We then administered salbutamol to *Lama1*$^{+/-}$ females crossed with *Lama1*$^{+/-}$ males to test if the deformed shape of *Lama1*$^{-/-}$ embryos could be restored by reducing the intrauterine pressure (Figures 6U–6X). We quantified embryonic shapes by measuring the angular differences of wild-type embryos and found that embryonic deformation was not evident after salbutamol administration (Figures 6V and 6X). Next, we analyzed the extent of deformation in *Lama1*$^{-/-}$ embryos and found that the deformation was considerably restored to that of the normal wild-type condition by salbutamol administration (Figures 6W and 6X). These findings indicated that even in the absence of RM, a moderate reduction in intrauterine pressures was sufficient for proper egg-cylinder morphogenesis.

Finally, to verify whether the buffer space created by RM is crucial to protect embryos against external forces, we placed a quantitative mechanical stress on a wild-type embryo using a 30-μm-diameter bead on an atomic force microscope (AFM) cantilever tip (Figure 7A). Using the cantilever, wild-type embryos that were completely sealed by RM did not collapse after a 30-nN compression (Figures 7B and 7C). In contrast, when we placed an identical external stress on wild-type embryos with an AFM indentation, in which their RM was completely removed by fine forceps (Figure 7D), the embryonic shape was clearly deformed locally (Figures 7E and 7F). We then artificially pierced a hole in the RM of wild-type embryos to recapitulate the situation of *Fktn*$^{-/-}$ embryos so that the buffer space constructed by RM was lost (Figures 4 and 7G). Thereafter, we similarly placed an identical external stress on these embryos by AFM indentation (Figures 7G–7I). Notably, wild-type embryos with a pierced RM collapsed even where the cantilever locally compressed the embryo indirectly via RM (Figures 7H and 7I). These findings demonstrated that a quantitative and local mechanical stress was not able to deform the morphology of wild-type embryos that had a completely sealed space with RM. However, an external stress deformed the embryonic shape when the sealed buffer space with wild-type RM was incomplete. Therefore, this finding also demonstrated that not only punctured *Fktn*$^{-/-}$ RM but also punctured wild-type RM was unable to protect embryos from external mechanical forces. Taken together, these results clearly support the notion that the blank space sealed by RM plays an essential role in moderately cushioning and dispersing intrauterine pressures for correct egg-cylinder morphogenesis.

DISCUSSION

Our studies have clearly delineated how the mechanical environment of the uterus is necessary for mouse egg-cylinder morphogenesis (Figure S7A). This involves a morphogenetic change from the spherical shape of a preimplanted blastocyst to the egg-cylinder shape of an implanted embryo during early implantation stages (Figure S7B). Additionally, this might highlight how prolific rodents can utilize their uterine space more effectively, because the direction of an embryo is destined to be perpendicular to that of uterine horns (Smith, 1985).

(C–P) Whole-mount *in situ* hybridization of *Bmp4* (C and D), *Cdx2* (E and F) mRNA markers for extraembryonic ectoderm; *Oct4* (G and H) mRNA, a marker for epiblasts; and *Cer1* (I and J), *Hex* (K and L), *Lhx1* (M and N), and *Lefty1/2* (O and P) mRNA markers for distal visceral endoderm (DVE)/anterior VE (AVE) of wild-type embryos that developed in uteri treated with PBS as a control (C, E, G, I, K, M, and O) and salbutamol (D, F, H, J, L, N, and P) at E5.75.

(Q–T) Immunohistochemical analyses using paraffin sections in wild-type uteri treated with PBS (Q and S) or salbutamol (R and T) at E5.75. SOX17 (green) (Q and R) with nuclei (DAPI, blue) (S and T). SOX17 was expressed in entire VE cells in both PBS- (Q and S) and salbutamol-treated (R and T) embryos.

(U) A schematic schedule of the administration of salbutamol or PBS (as a control) to *Lama1*$^{+/-}$ mothers and the collection of embryos to measure their angular differences, with or without salbutamol.

(V and W) Immunohistochemistry of EOMES (green) merged with nuclei (DAPI, blue); dashed white lines represent embryonic shapes, and dashed red lines represent the border between the epiblast and EOMES-positive extraembryonic ectoderm of wild-type (V) and *Lama1*$^{-/-}$ (W) embryos at E6.5, with PBS (left) or salbutamol (right) treatment. Yellow polygonal lines connect three points (the most distal center, the center of the boundary between the epiblast and extraembryonic ectoderm [magenta dashed lines], and the most proximal center), corresponding to normal or deformed shapes of embryos.

(X) Degrees of angular differences of wild-type and *Lama1*$^{-/-}$ embryos, with or without salbutamol. The deformation of *Lama1*$^{-/-}$ embryos appeared to be restored. Green lines indicate the mean value, and red lines represent the SE (one-way ANOVA followed by Tukey–Kramer, n.s., not significant, $p = 0.99$; wild-type embryo without salbutamol versus wild-type embryos with salbutamol, $p = 0.36$; wild-type embryos with salbutamol versus *Lama1*$^{-/-}$ embryos with salbutamol, $^{**}p < 0.01$). n = 7 (wild-type embryos without salbutamol), n = 7 (wild-type embryos with salbutamol), n = 8 (*Lama1*$^{-/-}$ embryos without salbutamol), and n = 8 (*Lama1*$^{-/-}$ embryos with salbutamol) at E6.5.

Scale bars represent 50 μm (C–T) and 100 μm (V and W). Images are representative of analyzed embryos (Table S6). See also Figure S5–S7 and Tables S4 and S5.

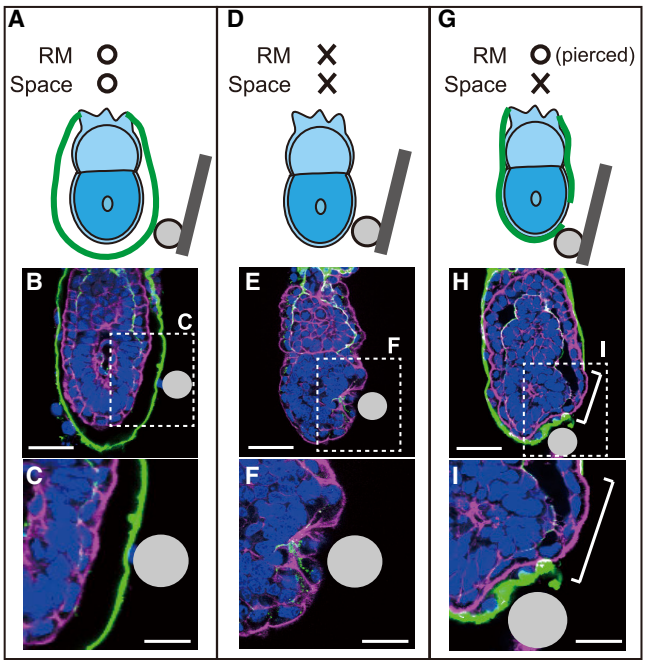

Figure 7. Manipulations of the Force Exerted on RM-Defective Embryos Affect Egg-Cylinder Morphology

(A, D, and G) Schematic illustrations of local indentation experiments *ex utero* using an atomic force microscope (AFM) with a wild-type embryo wrapped by RM (in green) (A), a wild-type embryo completely without RM (D), and a wild-type embryo in which RM (in green) is artificially pierced with a fine needle (G).

(B, E, and H) Immunohistochemistry of laminin subunit α1 (LAMA1; green), F-actin (phalloidin, magenta), and nuclei (DAPI, blue) of embryos after local indentation as illustrated above (A, D, and G).

(C, F, and I) Higher magnifications of white quadrated areas are shown in (B), (E), and (H), respectively. The light gray circle indicates the nearly identical size of the glass bead attached to a cantilever tip (30 μm diameter).

Scale bars represent 50 μm (B, E, and H) and 25 μm (C, F, and I). Images are representative of analyzed embryos (Table S6). See also Figure S7.

Current findings revealed that uterine smooth muscle contractions produced high and periodic intrauterine pressures during egg-cylinder morphogenesis in the mouse (Figure 5). In a mouse pregnancy, uterine muscle contraction is a crucial factor for the transfer and delivery of embryos. In the early period of embryogenesis, fertilized eggs are conveyed from oviducts to the uterus to be implanted in the uterus. Disturbance of intrauterine contractions at the preimplantation stage causes the aberrant distribution of implanted embryos (Chen et al., 2011). At the end of embryogenesis, uterine muscle contractions deliver embryos, which is also known as labor (Rada et al., 2015; Robuck et al., 2018). Inappropriate uterine muscle contractions cause preterm or delayed labor (Pierce et al., 2008, 2010; Bond et al., 2000; Padol et al., 2017). Except for these two events, however, no evidence exists on how uterine muscle contractions contribute to embryonic development. In this study, we revealed that the amplitude of intrauterine pressures was the highest and most frequent at E5.5 just after implantation (Figure 5). Relaxation of uterine smooth muscle contractions by salbutamol reduced the amplitude of the intrauterine pressure and thereby restored the correct egg-cylinder shape in deformed *Lama1*$^{-/-}$ mutant embryos (Figures 6U–6X). Thus, intrauterine pressures produced by smooth muscle contractions appear to contribute to early egg-cylinder morphogenesis. Moreover, the current study also implies that mechanical imbalances among the embryo, decidua, and uterine muscle contractions may adversely affect early embryogenesis *in utero* and thereby might result in spontaneous abortion at an early stage of mammalian pregnancy.

Given that external mechanical cues trigger elongation of the egg-cylinder shape along a proximo-distal orientation (Hiramatsu et al., 2013), it may be reasonable to presume that intrauterine pressures are also involved in the early polarization of the A-P axis (i.e., DVE formation), supporting the presence of a clear non-embryo-autonomous mechanism. In agreement with this assumption, the relaxation of uterine smooth muscle contractions with salbutamol disturbed the correct formation of the A-P axis (i.e., DVE specification) (Figures 6I–6P). A reduction in intrauterine pressures failed to induce DVE markers properly, although SOX-17-positive VE cells were normally differentiated (Figures 6Q–6T). Thus, it may be considered that intrauterine pressures reduced by salbutamol are insufficient to specify DVE correctly, since DVE is induced by the transmigration of epiblast cells by breaching the embryonic BM between the epiblast and VE (Hiramatsu et al., 2013). However, AVE emerged by a later E6.5 (Figure S6S). This restoration may be due to the relatively short duration of the clinical effect of salbutamol, and lower but continue, intrauterine pressures would be sufficient for the longitudinal elongation of the egg-cylinder shape, which results in DVE specification, as previously proposed (Hiramatsu et al., 2013; Matsuo and Hiramatsu, 2017).

The present study showed that RM plays a unique mechanical role in cushioning the intrauterine pressure exerted on embryos. Although RM was thought to exchange gases and nutrients between embryos and the uterus through a liquid-like amniotic fluid (Hogan et al., 1984; Jollie, 1968), additional roles for RM in embryogenesis have been identified in this study. More mechanistically, the sealed buffer space between embryos and maternal tissues created by RM was crucial in acting as an absorber, dispersing locally concentrated stress (Figures 3, 6, and 7). Consequently, a vulnerable RM, which is unable to make buffer space, as observed in *Fktn*$^{-/-}$ embryos, resulted in distorted egg-cylinder morphogenesis (Figures 4 and S2). Thus, we propose that this buffering mechanism is necessary and a prerequisite for subsequent egg-cylinder morphogenesis (Figure S7B). However, unsolved issues remain to be addressed, including how intrauterine pressures, RM, decidua, and the embryo itself interact each with other to elongate the egg-cylinder toward the distal side. Therefore, in addition to the buffering role of RM, other important mechanisms may be involved in the elongation of the egg-cylinder shape. To explore these issues explicitly, further intensive biomechanical, morphological, and genetic studies will be necessary.

STAR★METHODS

Detailed methods are provided in the online version of this paper and include the following:

- KEY RESOURCES TABLE

SUPPLEMENTAL INFORMATION

Supplemental Information can be found online at https://doi.org/10.1016/j.celrep.2020.107637.

ACKNOWLEDGMENTS

We are grateful to Drs. E. DeRobertis, J.A. Belo, H. Schöler, B.L. Hogan, R. Beddington, J. Deschamps, H. Hamada, and B.G. Herrmann for plasmids and Dr. I. Nishii and Messrs. K. Debari and E. Oiki for technical support with transmission electron microscopy. The monoclonal antibodies against dystroglycan α (IIH6C4) and dystroglycan β (7D11) were developed by K.P. Campbell and G.E. Morris, obtained from the Developmental Studies Hybridoma Bank, created by the NICHD of the NIH, and maintained at the Department of Biology, The University of Iowa, Iowa City, IA 52242.

This work was supported in part by grants-in-aid for Scientific Research on Priority Areas and on Innovative Areas (JP18H04771 and JP19H04798) and Scientific Research (B) (JP19H03238), (C) (JP17K10202) from the Ministry of Education, Culture, Sports, Science, and Technology, Japan; a Sukoyaka grant for maternal and child health, Japan; the Naito Foundation, Japan; and the Takeda Science Foundation, Japan. The funders had no role in the study design, data collection and analysis, decision to publish, or preparation of the manuscript.

AUTHOR CONTRIBUTIONS

Y.U., C.K.-Y., R.H., and I.M. initiated the research and planned the experiments. Y.U., K.M., M.T., and R.H. performed the experiments. Y.K. and T.A. discussed mechanical methods and data. O.L. provided *Lama1* mutant mice and discussed statistical data. Y.U., C.K.-Y., and I.M. contributed to the writing of the manuscript.

DECLARATION OF INTERESTS

The authors declare no competing interests.

Received: November 14, 2019
Revised: March 10, 2020
Accepted: April 21, 2020
Published: May 19, 2020

REFERENCES

Alpy, F., Jivkov, I., Sorokin, L., Klein, A., Arnold, C., Huss, Y., Kedinger, M., Simon-Assmann, P., and Lefebvre, O. (2005). Generation of a conditionally null allele of the laminin alpha1 gene. Genesis *43*, 59–70.

Barnes, J.D., Crosby, J.L., Jones, C.M., Wright, C.V., and Hogan, B.L. (1994). Embryonic expression of Lim-1, the mouse homolog of Xenopus Xlim-1, suggests a role in lateral mesoderm differentiation and neurogenesis. Dev. Biol. *161*, 168–178.

Beccari, L., Moris, N., Girgin, M., Turner, D.A., Baillie-Johnson, P., Cossy, A.C., Lutolf, M.P., Duboule, D., and Arias, A.M. (2018). Multi-axial self-organization properties of mouse embryonic stem cells into gastruloids. Nature *562*, 272–276.

Beddington, R.S., and Robertson, E.J. (1999). Axis development and early asymmetry in mammals. Cell *96*, 195–209.

Bedford, F.K., Ashworth, A., Enver, T., and Wiedemann, L.M. (1993). HEX: a novel homeobox gene expressed during haematopoiesis and conserved between mouse and human. Nucleic Acids Res. *21*, 1245–1249.

Bedzhov, I., and Zernicka-Goetz, M. (2014). Self-organizing properties of mouse pluripotent cells initiate morphogenesis upon implantation. Cell *156*, 1032–1044.

Bedzhov, I., Leung, C.Y., Bialecka, M., and Zernicka-Goetz, M. (2014). In vitro culture of mouse blastocysts beyond the implantation stages. Nat. Protoc. *9*, 2732–2739.

Beedle, A.M., Turner, A.J., Saito, Y., Lueck, J.D., Foltz, S.J., Fortunato, M.J., Nienaber, P.M., and Campbell, K.P. (2012). Mouse *fukutin* deletion impairs dystroglycan processing and recapitulates muscular dystrophy. J. Clin. Invest. *122*, 3330–3342.

Belo, J.A., Bouwmeester, T., Leyns, L., Kertesz, N., Gallo, M., Follettie, M., and De Robertis, E.M. (1997). Cerberus-like is a secreted factor with neutralizing activity expressed in the anterior primitive endoderm of the mouse gastrula. Mech. Dev. *68*, 45–57.

Bier, E., and De Robertis, E.M. (2015). EMBRYO DEVELOPMENT. BMP gradients: a paradigm for morphogen-mediated developmental patterning. Science *348*, aaa5838.

Bond, C.T., Sprengel, R., Bissonnette, J.M., Kaufmann, W.A., Pribnow, D., Neelands, T., Storck, T., Baetscher, M., Jerecic, J., Maylie, J., et al. (2000). Respiration and parturition affected by conditional overexpression of the Ca2+-activated K+ channel subunit, SK3. Science *289*, 1942–1946.

Charras, G., and Sahai, E. (2014). Physical influences of the extracellular environment on cell migration. Nat. Rev. Mol. Cell Biol. *15*, 813–824.

Chen, Q., Zhang, Y., Peng, H., Lei, L., Kuang, H., Zhang, L., Ning, L., Cao, Y., and Duan, E. (2011). Transient beta2-adrenoceptor activation confers pregnancy loss by disrupting embryo spacing at implantation. J. Biol. Chem. *286*, 4349–4356.

Copp, A.J. (1979). Interaction between inner cell mass and trophectoderm of the mouse blastocyst. II. The fate of the polar trophectoderm. J. Embryol. Exp. Morphol. *51*, 109–120.

Desaki, J., and Uehara, Y. (1981). The overall morphology of neuromuscular junctions as revealed by scanning electron microscopy. J. Neurocytol. *10*, 101–110.

Dumont, J.N., and Brummett, A.R. (1985). Egg envelopes in vertebrates. Dev. Biol. *1*, 235–288.

Edwards, M.M., Mammadova-Bach, E., Alpy, F., Klein, A., Hicks, W.L., Roux, M., Simon-Assmann, P., Smith, R.S., Orend, G., Wu, J., et al. (2010). Mutations in *Lama1* disrupt retinal vascular development and inner limiting membrane formation. J. Biol. Chem. *285*, 7697–7711.

Eiraku, M., Takata, N., Ishibashi, H., Kawada, M., Sakakura, E., Okuda, S., Sekiguchi, K., Adachi, T., and Sasai, Y. (2011). Self-organizing optic-cup morphogenesis in three-dimensional culture. Nature *472*, 51–56.

Evan, A.P., Dail, W.G., Dammrose, D., and Palmer, C. (1976). Scanning electron microscopy of cell surfaces following removal of extracellular material. Anat. Rec. *185*, 433–445.

Grotegut, C.A., Mao, L., Pierce, S.L., Swamy, G.K., Heine, R.P., and Murtha, A.P. (2016). Enhanced uterine contractility and stillbirth in mice lacking G protein-coupled receptor kinase 6 (GRK6): implications for oxytocin receptor desensitization. Mol. Endocrinol. *30*, 455–468.

Grove, E.A., Tole, S., Limon, J., Yip, L., and Ragsdale, C.W. (1998). The hem of the embryonic cerebral cortex is defined by the expression of multiple Wnt genes and is compromised in Gli3-deficient mice. Development *125*, 2315–2325.

Herrmann, B.G. (1991). Expression pattern of the Brachyury gene in whole-mount TWis/TWis mutant embryos. Development *113*, 913–917.

Hiramatsu, R., Matsuoka, T., Kimura-Yoshida, C., Han, S.W., Mochida, K., Adachi, T., Takayama, S., and Matsuo, I. (2013). External mechanical cues trigger the establishment of the anterior-posterior axis in early mouse embryos. Dev. Cell *27*, 131–144.

Hogan, B.L., Cooper, A.R., and Kurkinen, M. (1980). Incorporation into Reichert's membrane of laminin-like extracellular proteins synthesized by parietal endoderm cells of the mouse embryo. Dev. Biol. *80*, 289–300.

Hogan, B.L., Barlow, D.P., and Kurkinen, M. (1984). Reichert's membrane as a model for studying the biosynthesis and assembly of basement membrane components. Ciba Found. Symp. *108*, 60–74.

Hsu, Y.C. (1973). Differentiation in vitro of mouse embryos to the stage of early somite. Dev. Biol. *33*, 403–411.

Ichikawa-Tomikawa, N., Ogawa, J., Douet, V., Xu, Z., Kamikubo, Y., Sakurai, T., Kohsaka, S., Chiba, H., Hattori, N., Yamada, Y., and Arikawa-Hirasawa, E. (2012). Laminin α1 is essential for mouse cerebellar development. Matrix Biol. *31*, 17–28.

Jollie, W.P. (1968). Changes in the fine structure of the parietal yolk sac of the rat placenta with increasing gestational age. Am. J. Anat. *122*, 513–531.

Jones, C.M., Lyons, K.M., and Hogan, B.L. (1991). Involvement of bone morphogenetic protein-4 (BMP-4) and Vgr-1 in morphogenesis and neurogenesis in the mouse. Development *111*, 531–542.

Kimura, C., Yoshinaga, K., Tian, E., Suzuki, M., Aizawa, S., and Matsuo, I. (2000). Visceral endoderm mediates forebrain development by suppressing posteriorizing signals. Dev. Biol. *225*, 304–321.

Kimura-Yoshida, C., Mochida, K., Ellwanger, K., Niehrs, C., and Matsuo, I. (2015). Fate specification of neural plate border by canonical Wnt signaling and Grhl3 is crucial for neural tube closure. EBioMedicine *2*, 513–527.

Kurahashi, H., Taniguchi, M., Meno, C., Taniguchi, Y., Takeda, S., Horie, M., Otani, H., and Toda, T. (2005). Basement membrane fragility underlies embryonic lethality in fukutin-null mice. Neurobiol. Dis. *19*, 208–217.

Ladoux, B., and Mège, R.M. (2017). Mechanobiology of collective cell behaviours. Nat. Rev. Mol. Cell Biol. *18*, 743–757.

Leivo, I., Vaheri, A., Timpl, R., and Wartiovaara, J. (1980). Appearance and distribution of collagens and laminin in the early mouse embryo. Dev. Biol. *76*, 100–114.

Matsuo, I., and Hiramatsu, R. (2017). Mechanical perspectives on the anterior-posterior axis polarization of mouse implanted embryos. Mech. Dev. *144* (*Pt A*), 62–70.

Meno, C., Saijoh, Y., Fujii, H., Ikeda, M., Yokoyama, T., Yokoyama, M., Toyoda, Y., and Hamada, H. (1996). Left-right asymmetric expression of the TGF beta-family member lefty in mouse embryos. Nature *381*, 151–155.

Mesnard, D., Guzman-Ayala, M., and Constam, D.B. (2006). Nodal specifies embryonic visceral endoderm and sustains pluripotent cells in the epiblast before overt axial patterning. Development *133*, 2497–2505.

Nagy, A.G.M., Vintersten, K., and Behringer, R. (2014). Manipulating of the Mouse Embryo. A Laboratory Manual, Fourth Edition (Cold Spring Harbor Laboratory Press).

Niehrs, C. (2010). On growth and form: a Cartesian coordinate system of Wnt and BMP signaling specifies bilaterian body axes. Development *137*, 845–857.

Padol, A.R., Sukumaran, S.V., Sadam, A., Kesavan, M., Arunvikram, K., Verma, A.D., Srivastava, V., Panigrahi, M., Singh, T.U., Telang, A.G., et al. (2017). Hypercholesterolemia impairs oxytocin-induced uterine contractility in late pregnant mouse. Reproduction *153*, 565–576.

Pierce, S.L., Kresowik, J.D., Lamping, K.G., and England, S.K. (2008). Overexpression of SK3 channels dampens uterine contractility to prevent preterm labor in mice. Biol. Reprod. *78*, 1058–1063.

Pierce, S.L., Kutschke, W., Cabeza, R., and England, S.K. (2010). In vivo measurement of intrauterine pressure by telemetry: a new approach for studying parturition in mouse models. Physiol. Genomics *42*, 310–316.

Pöschl, E., Schlötzer-Schrehardt, U., Brachvogel, B., Saito, K., Ninomiya, Y., and Mayer, U. (2004). Collagen IV is essential for basement membrane stability but dispensable for initiation of its assembly during early development. Development *131*, 1619–1628.

Rada, C.C., Pierce, S.L., Grotegut, C.A., and England, S.K. (2015). Intrauterine telemetry to measure mouse contractile pressure in vivo. J. Vis. Exp. *98*, e52541.

Robuck, M.F., O'Brien, C.M., Knapp, K.M., Shay, S.D., West, J.D., Newton, J.M., Slaughter, J.C., Paria, B.C., Reese, J., and Herington, J.L. (2018). Monitoring uterine contractility in mice using a transcervical intrauterine pressure catheter. Reproduction *155*, 447–456.

Salamat, M., Miosge, N., and Herken, R. (1995). Development of Reichert's membrane in the early mouse embryo. Anat. Embryol. (Berl.) *192*, 275–281.

Schöler, H.R., Ruppert, S., Suzuki, N., Chowdhury, K., and Gruss, P. (1990). New type of POU domain in germ line-specific protein Oct-4. Nature *344*, 435–439.

Smith, L.J. (1985). Embryonic axis orientation in the mouse and its correlation with blastocyst relationships to the uterus. II. Relationships from 4 1/4 to 9 1/2 days. J. Embryol. Exp. Morphol. *89*, 15–35.

Smith, K.K., and Strickland, S. (1981). Structural components and characteristics of Reichert's membrane, an extra-embryonic basement membrane. J. Biol. Chem. *256*, 4654–4661.

Srinivas, S., Rodriguez, T., Clements, M., Smith, J.C., and Beddington, R.S. (2004). Active cell migration drives the unilateral movements of the anterior visceral endoderm. Development *131*, 1157–1164.

Stern, C.D., and Downs, K.M. (2012). The hypoblast (visceral endoderm): an evo-devo perspective. Development *139*, 1059–1069.

Takaoka, K., Nishimura, H., and Hamada, H. (2017). Both Nodal signalling and stochasticity select for prospective distal visceral endoderm in mouse embryos. Nat. Commun. *8*, 1492.

Thomas, P., and Beddington, R. (1996). Anterior primitive endoderm may be responsible for patterning the anterior neural plate in the mouse embryo. Curr. Biol. *6*, 1487–1496.

Thomas, P.Q., Brown, A., and Beddington, R.S. (1998). Hex: a homeobox gene revealing peri-implantation asymmetry in the mouse embryo and an early transient marker of endothelial cell precursors. Development *125*, 85–94.

Vianello, S., and Lutolf, M.P. (2019). Understanding the mechanobiology of early mammalian development through bioengineered models. Dev. Cell *48*, 751–763.

Vining, K.H., and Mooney, D.J. (2017). Mechanical forces direct stem cell behaviour in development and regeneration. Nat. Rev. Mol. Cell Biol. *18*, 728–742.

Whitmore, C., Fernandez-Fuente, M., Booler, H., Parr, C., Kavishwar, M., Ashraf, A., Lacey, E., Kim, J., Terry, R., Ackroyd, M.R., et al. (2014). The transgenic expression of LARGE exacerbates the muscle phenotype of dystroglycanopathy mice. Hum. Mol. Genet. *23*, 1842–1855.

Wilkinson, D.G. (1998). In Situ Hybridization: A Practical Approach, Volume 196, 2nd Edition (Oxford University Press).

Young, T., Rowland, J.E., van de Ven, C., Bialecka, M., Novoa, A., Carapuco, M., van Nes, J., de Graaff, W., Duluc, I., Freund, J.N., et al. (2009). Cdx and Hox genes differentially regulate posterior axial growth in mammalian embryos. Dev. Cell *17*, 516–526.

STAR★METHODS

KEY RESOURCES TABLE

REAGENT or RESOURCE	SOURCE	IDENTIFIER
Antibodies		
Goat polyclonal anti-Laminin α-1	Santa Cruz	Cat#sc-6017; RRID: AB_2133628
Rabbit polyclonal anti-Collagen type IV	Millipore	Cat#AB756P; RRID: AB_2276457
Mouse monoclonal anti-Dystroglycan, alpha (IIH6c4)	DSHB	Cat#IIH6 C4; RRID: AB_2617216
Rat monoclonal anti-Nidogen	Santa Cruz	Cat#sc-33706; RRID: AB_627519
Rabbit polyclonal anti-TBR2 / Eomes	Abcam	Cat#ab23345; RRID: AB_778267
Goat polyclonal anti-Gata6	R&D systems	Cat# AF1700; RRID: AB_2108901
Rabbit polyclonal anti-Histone H3, phospho (Ser10)	Millipore	Cat# 06-570; RRID: AB_310177
Rabbit monoclonal anti-Cleaved Caspase-3 (Asp175)	Cell Signaling Technology	Cat# 9664; RRID: AB_2070042
Mouse monoclonal anti-MANDAG2 dystroglycan, beta	DSHB	Cat# MANDAG2 clone 7D11; RRID: AB_2211772
Rabbit polyclonal anti-Fukutin	Abcam	Cat#ab171195
Rabbit polyclonal anti-Cox-2	Cayman	Cat# 160107; RRID: AB_10078833
Rabbit monoclonal anti-phospho-Stat3 (Tyr705)	Cell Signaling Technology	Cat# 9145; RRID: AB_2491009
Goat polyclonal anti-Sox17	R&D systems	Cat# AF1924; RRID: AB_355060
Alexa 488-conjugated donkey anti-goat IgG antibody	Thermo Fisher Scientific	Cat# A-11055; RRID: AB_2534102
Alexa 488-conjugated rabbit anti-goat IgG antibody	Thermo Fisher Scientific	Cat# A-11078; RRID: AB_141838
Alexa 488-conjugated goat anti-mouse IgM antibody	Thermo Fisher Scientific	Cat# A-21042; RRID: AB_141357
Alexa 488-conjugated goat anti-mouse IgG1 antibody	Thermo Fisher Scientific	Cat# A-21121; RRID: AB_141514
Alexa 488-conjugated goat anti-rat IgG antibody	Thermo Fisher Scientific	Cat# A-11006; RRID: AB_141373
Alexa 568-conjugated donkey anti-rabbit IgG antibody	Thermo Fisher Scientific	Cat# A-10042; RRID: AB_2534017
Alexa 568-conjugated goat anti-rabbit IgG antibody	Thermo Fisher Scientific	Cat# A-11036; RRID: AB_143011
Alexa 568-conjugated rabbit anti-goat IgG antibody	Thermo Fisher Scientific	Cat# A-11079; RRID: AB_1500596
Chemicals, Peptides, and Recombinant Proteins		
Alexa Fluor 488 Phalloidin	Thermo Fisher Scientific	Cat#A-12379
DAPI	Lonza	Cat#PA-3013
DIG RNA labeling mix 10X	Roche Diagnostics GmbH	Cat#17109821
Salbutamol	Alfa Aesar	Cat#A-18544
Critical Commercial Assays		
TArget Clone™	TOYOBO	Cat#TAK-101
DNA Ligation Kit < Mighty Mix >	Takara	Cat#6023
Experimental Models: Organisms/Strains		
Mouse: ICR	CLEA Japan	Jcl:ICR
Mouse: C57BL/6J	CLEA Japan	C57BL/6JJcl
Mouse: *Lama1*$^{flox/flox}$	Alpy et al. (2005)	N/A
Mouse: *β-actin Cre*	Kimura-Yoshida et al., (2015)	N/A
Mouse: *Lama1*$^{+/-}$	Alpy et al. (2005)	N/A
Mouse: *Fktn*$^{rm1.Kcam}$	Jackson Laboratory Beedle et al., 2012	B6.129-Fktn < tm1Kcam > /J
Mouse: *Fktn*$^{+/-}$	Beedle et al., 2012	N/A
Oligonucleotides		
Ln150 5′-CCTGTTTAAAGGGCCAAACGGTACAGG	Hokkaido System Science	N/A
Ln151 5′-TCATTTTGGAAAAACTCGTTTTAAACC	Hokkaido System Science	N/A

(*Continued on next page*)

Continued

REAGENT or RESOURCE	SOURCE	IDENTIFIER
Lama1_RV2 5′-CAGGCTTTGTGGGGAGAGGGCAGAGGTGTC	Hokkaido System Science	N/A
Fktn_cre_for 5′-TCTTTAGTCAGCGTGGTCAGAAGTAGCATC	Hokkaido System Science	N/A
Fktn_flox_for 5′-GAAGTCAAGATACTGGGCTG	Hokkaido System Science	N/A
Fktn_Cre_rev 5′-AGCAGCAAGGGCCAAGAGGATATCTACAGT	Hokkaido System Science	N/A
For Lama1 cDNA forward 5′-CGGAGAGTTATCACCATACAAGTG	Hokkaido System Science	N/A
For Lama1 cDNA reverse 5′-CGCCTTCCTTTTAATGTATTCTGT	Hokkaido System Science	N/A
For Col IV cDNA forward 5′-GTCCAGGACCAAGTGGAAGA	Hokkaido System Science	N/A
For Col IV cDNA reverse 5′-GTCTCCTTTGTCACCTTTGAG	Hokkaido System Science	N/A
Recombinant DNA		
pTA2-Lama1	this paper	N/A
pTA2-Col IV1a	Hiramatsu et al. (2013)	N/A
pBS-Oct4	Schöler et al. (1990)	N/A
pBS-Cdx2	Young et al. (2009)	N/A
pSP72-Bmp4	Jones et al. (1991)	N/A
pBS-Hex	Bedford et al. (1993)	N/A
pBS-Cer1	Belo et al. (1997)	N/A
pBS-Lhx1	Barnes et al. (1994)	N/A
pBS-Lefty1/2	Meno et al. (1996)	N/A
pBS-Brachyury	Herrmann. (1991)	N/A
Software and Algorithms		
FV10-ASW4.2 viewer	Olympus	N/A
ImageJ	NIH	N/A
NRecon	Bruker	N/A
CT-Analyzer	Bruker	N/A
CT-volume	Bruker	N/A
Dataviewer	Bruker	N/A
LabScribe3	iWorx Systems	N/A
Nanowizard SPM software	JPK	N/A
Data Processing software	JPK	N/A
Other		
Confocal Laser Scanning Biological Microscope	Olympus	FV1000, FV3000
Ultramicrotome	Leica	Ultracut-UCT
Transmission electron microscope	JEOL	JEM-1400Plus
Scanning electron microscope	Hitachi	TM3030 Plus
Micro-Computed tomography	Bruker	SKYSCAN1272
Pressure Catheter (1.2Fr; single)	Transonic	Cat#FTH-1211B-0018
SP200 Pressure Control Unit	iWorx Systems	Cat#FP095B
Atomic force microscopy	JPK	NanoWizard4
Inverted microscope	Olympus	IX73, IX83
CCD camera	Andor Technology	Zyla5.5

RESOURCE AVAILABILITY

Lead Contact

Further information and requests for resources and reagents should be directed to and fulfilled by the Lead Contact, Isao Matsuo (imatsuo@wch.opho.jp).

Materials Availability

This study did not generate new unique reagents except the plasmid pTA2-Lama1. This plasmid is available from the corresponding author upon request.

Data and Code Availability

This study did not generate datasets/code and the published article included all data analyzed during this study. All relevant data are available from the corresponding author upon reasonable request.

EXPERIMENTAL MODEL AND SUBJECT DETAILS

All mouse studies followed fundamental guidelines for the proper conduct of animal experiments and related activities in academic research institutions under the jurisdiction of the Ministry of Education, Culture, Sports, Science and Technology in Japan and were approved by institutional committees at the Research Institute for Osaka Women's and Children's Hospital for animal and recombinant DNA experiments. Female and male mice were used at 3-7 months of age for mating. We collected and analyzed embryos from both male and female randomly without sex determination to eliminate sex differences.

METHOD DETAILS

Mutant Mice

Lama1$^{+/-}$ mice were generated by mating *Lama1*$^{flox/flox}$ mice (obtained from Inserm U1109, Strasbourg, France) (Alpy et al., 2005), with *β-actin Cre* transgenic mice (Kimura-Yoshida et al., 2015). The resulting *Lama1*$^{+/-}$ mice were maintained in a ICR background. *Lama1* null mutant mice were identified with three primers: Ln150, Ln151 and Lama1_RV2 (Key Resources Table), yielding 315 bp as the wild-type allele and 505 bp as the mutant allele.

To obtain *Fktn*$^{+/-}$ mice, *in vitro* fertilization was performed using the sperm of a heterozygous *Fktn*$^{tm1.Kcam}$ mouse (obtained from The Jackson Laboratory, Bar Harbor, ME, USA; Beedle et al., 2012) and the oocytes of a *β-actin Cre* mouse. *In vitro* fertilized oocytes were transferred to pseudopregnant recipients according to standard methods (Nagy et al., 2014). The resulting *Fktn*$^{+/-}$ mice were maintained in C57BL/6J genetic background. *Fktn* null mutant mice were identified with three primers: Fktn_cre_for, Fktn_flox_for and Fktn_Cre_rev (Key Resources Table), yielding 223 bp as the wild-type allele and 438 bp as the mutant allele.

Immunohistochemistry

For whole-mount immunohistochemistry, embryos at E4.5 to E6.5 were fixed overnight in 4% paraformaldehyde in phosphate buffered saline (PBS) followed by a brief wash in 0.1% Triton X-100 in PBS (PBST). Antigen retrieval was done by heating in HistoVT One antigen retrieval solution (Nakalai Tesque Inc, Kyoto, Japan) in an autoclave. The embryos were incubated in blocking solution (1% bovine serum albumin, 10% goat or rabbit or donkey serum in PBST) for 2 h, then immersed overnight at 4°C in primary antibody solution diluted in blocking solution (Key Resources Table). The embryos were washed eight times in PBST, for 20 min per wash, and incubated with appropriate species-specific fluorophore-conjugated secondary antibodies (Invitrogen, Carlsbad, CA, USA) overnight at 4°C. The nuclei were stained with DAPI (Lonza, Basel, Switzerland). F-actin was stained with Alexa Fluor 488 phalloidin (Molecular Probes, Eugene, OR, USA). Staining was examined with a confocal microscope (Olympus FV1000 and FV3000; Olympus, Tokyo, Japan). Figure images are representative of analyzed embryos described in Table S6.

Histology and *in situ* Hybridization

For histological analysis, embryos with decidual tissues were fixed in Bouin's solution for morphological analysis, in 4% paraformaldehyde solution in PBS for immunohistochemistry and *in situ* hybridization, then dehydrated and embedded in paraplast. Serial sections (thickness, 7 μm) were generated and stained with hematoxylin and eosin. *Lama1* and *Col41a* plasmids for *in situ* probes were constructed as follows: Two primer sets, For *Lama1* cDNA forward and For *Lama1* cDNA forward reverse, For *Col41a* cDNA forward and For *Col41a* cDNA reverse (Key Resources Table), were used for PCR amplification. The amplified 660 bp for *Lama1* and 425 bp for *Col41a*, respectively, were subcloned into a pTA2 vector. *Oct4*, *Cdx2*, *Bmp4*, *Hex, Lhx1, Lefty1/2, Brachyury* and *Cer1,* plasmids for *in situ* hybridization were obtained from Drs. H. Schöler, J. Deschamps, B.L. Hogan, H. Hamada, B.G. Herrmann, R. Beddington and E. DeRobertis, J.A. Belo, respectively (Key Resources Table). *In situ* hybridization involving digoxigenin-labeled probes was conducted as described previously (Grove et al., 1998; Wilkinson, 1998). Figure images are representative of analyzed embryos described in Table S6.

Transmission Electron Microscopy

For fine ultrastructure analysis, embryos with decidual tissues were fixed overnight in 2% paraformaldehyde plus 2.5% glutaraldehyde in 0.1 M sodium cacodylate buffer (pH 7.3) at 4°C. The tissues were postfixed for 1 h in 1% OsO_4 at room temperature (RT), then dehydrated and replaced with propylene oxide, followed by embedding in Poly Bet 812. Ultrathin sections (70 nm thickness) were cut with an ultramicrotome (Ultracut UCT, Leica, Wetzlar, Germany) using a diamond knife. The specimens were stained with lead citrate and examined under a JEM-1400Plus electron microscope (JEOL, Tokyo, Japan).

Scanning Electron Microscopy

Uteruses were fixed in 4% paraformaldehyde solution in PBS overnight at 4°C. To remove the intramuscular connective tissue components, a method previously described by Evan et al. was partly modified and used (Desaki and Uehara, 1981; Evan et al., 1976). Fixed uteruses were rinsed in distilled water and then treated with 8 N HCl for 20 min at 60°C. After treatment, uteruses were rinsed in distilled water, then stained with TI Blue (Platinum Blue; Nisshin EM, Tokyo, Japan) for 30 min at RT and examined in a TM3030 Plus scanning electron microscope (SEM; Hitachi, Tokyo, Japan).

Micro-computed Tomography

Each uterus was cut off parallel to a mesometrial to anti-mesometrial direction as one decidual unit, including surrounding myometrium, and fixed in 4% paraformaldehyde solution in PBS for 48 h at 4°C. Fixed uterine fragments were washed in water, then immersed in 0.1 N iodine solution (Sigma, St Louis, MI, USA) for 48 h at RT with gentle rocking. Uterine fragments were then placed in microtubes to be scanned with a SKYSCAN 1272 micro-computed tomography (CT) scanner (Bruker, Kontich, Belgium), taking 1400 views in 75 min (1.5 μm/pixel resolution). The obtained data were analyzed with Data Viewer software, CT-Analyzer and CT-volume software (Bruker) for three dimensional reconstructions. Gray scale images indicate gray values ranging from 0 to 255. After scanning, samples were immersed in 6 mM thiosulfate (Nakalai Tesque Inc, Kyoto, Japan) in PBT for overnight at RT to remove the iodine solution, and then the embryos removed from decidua were subjected for genotyping by PCR with appropriate primers described Key Resources Table.

Intrauterine Pressure Measurement

Intrauterine pressures were measured with a 1.2 F microtransducer-mounted pressure catheter (FTH-1211B-0018; Transonic, Ithaca, NY, USA). Timed-pregnant mice were anesthetized by intraperitoneal delivery of a mixture of medetomidine hydrochloride (9 μg/30 g body), midazolam (120 μg/30 g body) and butorphanol tartrate (150 μg/30 g body). For abdominal operation, an incision was made in the abdominal wall to partially expose one side of the uterine horn. A hole was made from the anti-mesometrial side toward the mesometrial side with a 26G needle. Then, the catheter was carefully inserted into the above hole of the uterus along with mesometrial to anti-mesometrial axis in an orthogonal direction to the uterine longitudinal axis, i.e., oviduct to cervix axis. For transcervical insertion, the catheter was carefully inserted transcervically guided with 18G needle. After a few minutes of catheter insertion, when uterine contractions appeared to be constant, the uterine pressure was recorded with a SP200 Pressure control unit (FP095B; iWorx Systems, Dover, NH, USA) for 10 min under anesthesia. Then, data were analyzed using LabScribe3 software (iWorx Systems). Baseline (0 mmHg) was adjusted in PBS prior to the insertion of the catheter into uterine tissue, including decidua compression and uterine muscle contraction, at each embryonic stage. The whole intrauterine pressure, involving uterine contractions exerted on decidua, was assessed by previously described methods (Robuck et al., 2018): mean amplitude and frequency, area under the curve (AUC) and Montevideo units (the sum of amplitudes during a 10 minute period of time).

Atomic Force Microscopy

All atomic force microscopy (AFM) experiments were carried out with NanoWizard 4 (JPK Instruments, Berlin, Germany) controlled by AFM software (JPK Instruments). The head unit and stage of the atomic force microscope were both mounted on an inverted microscope (IX73; Olympus, Tokyo, Japan) and laser alignment was achieved with a CCD camera (Zyla5.5; Andor Technology, Belfast, UK). For extrinsic compression experiments using AFM, tipless cantilevers (AIOAL-TL-10; BudgetSensors, Sophia, Bulgaria) glued with 30-μm diameter glass beads were used. A sustained force of 30 nN was applied to compress E5.5 living embryos in DMEM (Life Technologies) supplemented with 10% fetal bovine serum (Hyclone, Thermo Scientific) for 10 min after their RM were left intact, completely removed and pierced.

Salbutamol Treatments

Salbutamol (Alfa Aesar, Haverhill, MA, USA) was prepared in PBS and administered at 4 mg/30 g body in total at every injection. The drug was administered by intraperitoneal injection at appropriate schedules. The control group mice received PBS only. The mice were bred with a light-dark cycle of light-on from 07:00 to 19:00 and light-off from 19:00 to 07:00. Implantation occurred at around E4.5, from 09:00 to15:00 on the fourth day after fertilization (day of plug). Three times administration of salbutamol started at 0:00 on the fifth day after fertilization (E5.0) then every 6 hours until 12:00 noon on the same day (E5.25 and E5.5, respectively).

QUANTIFICATION AND STATISTICAL ANALYSIS

Definition of statistical significance and size of *n* is indicated in Figure Legends and Table S6. All representative data and images were obtained from more than two independent experiments. The data are presented as the mean ± standard error (SE). Statistical analysis methods include Mann–Whitney's two-tailed *U*-test, and with one-way ANOVA followed by Tukey-Kramer.